Compositional editing of extracellular matrices by CRISPR/Cas9 engineering of human mesenchymal stem cell lines

Sujeethkumar Prithiviraj [1,2,3], Alejandro Garcia Garcia [1,2,3], Karin Linderfalk [1,2,3], Bai Yiguang [4], Sonia Ferveur [1,2,3], Ludvig Nilsén Falck [5], Agatheeswaran Subramaniam [5], Sofie Mohlin [6], David Hidalgo [1, 2,3], Steven J Dupard[1, 2,3], Dimitra Zacharaki[1,2,3], Deepak Bushan Raina [7], Paul E Bourgine [1,2,3].

[1]Cell, Tissue & Organ engineering laboratory, BMC B11, 22184, Department of Clinical Sciences, Lund Stem Cell Centre, Lund University, Lund, Sweden

[2]Wallenberg Centre for Molecular Medicine, Lund University, Lund, Sweden

[3]Lund University Cancer Centre, Lund University, Lund, Sweden

[4]Department of Orthopaedics, Nanchong central hospital, The second clinical Institute of North Sichuan Medical college Nanchong, Sichuan, China

[5]Division of Molecular Medicine and Gene Therapy, Lund Stem Cell Centre, Lund University, 22184 Lund, Sweden

[6]Division of Pediatrics, Clinical Sciences, Translational Cancer Research, Lund University Cancer Center at Medicon Village, Lund, 22363, Sweden

[7]The Faculty of Medicine, Department of Clinical Sciences Lund, Orthopedics, Lund 221 84, Sweden

Abstract

Tissue engineering strategies predominantly rely on the production of living substitutes, whereby implanted cells actively participate in the regenerative process. Beyond cost and delayed graft availability, the patient-specific performance of engineered tissues poses serious concerns on their clinical translation ability. A more exciting paradigm consists in exploiting cell-laid, engineered extracellular matrices (eECM), which can be used as off-the-shelf materials. Here, the regenerative capacity solely relies on the preservation of the eECM structure and embedded signals to instruct an endogenous repair. We recently described the possibility to exploit custom human stem cell lines for eECM manufacturing. In addition to the conferred standardization, the availability of such cell lines opened avenues for the design of tailored eECMs by applying dedicated genetic tools. In this study, we demonstrated the exploitation of CRISPR/Cas9 as a high precision system for editing the composition and function of eECMs. Human mesenchymal stromal/stem cell (hMSC) lines were modified to knockout VEGF and RUNX2 and assessed for their capacity to generate osteoinductive cartilage matrices. We report the successful editing of

32 hMSCs, subsequently leading to targeted VEGF and RUNX2-knockout cartilage eECMs. Despite the
33 absence of VEGF, eECMs retained full capacity to instruct ectopic endochondral ossification. Conversely,
34 RUNX2-edited eECMs exhibited impaired hypertrophy, reduced ectopic ossification and superior cartilage
35 repair in a rat osteochondral defect. In summary, our approach can be harnessed to identify the necessary
36 eECM factors driving endogenous repair. Our work paves the road towards the compositional eECMs
37 editing and their exploitation in broad regenerative contexts.

38

39 **Introduction**

40 Extracellular matrices (ECMs) are complex networks of proteins providing tissue structural and mechanical
41 support, but also acting as growth factor storing and presenting entities[1]. As such, ECMs are receiving
42 increasing attention in tissue engineering as templates capable of guiding homeostasis, remodeling, and
43 regenerative processes[2,3,4].
44 ECMs can be derived from native tissue or organs (native ECMs, nECMs) by applying a decellularization
45 step which effectively removes the cellular fraction. The resulting nECMs are commonly used as
46 biomaterials in regenerative medicine[5,6], offering a natural biocompatible structure. However, they suffer
47 from substantial batch-to-batch variation with their properties being largely affected by the tissue source
48 and the decellularization process[5,7]. Importantly, while displaying a high level of biological complexity and
49 fidelity, the composition of nECMs cannot be tailored to specific needs.
50 A valuable option emerged from recent advances in bioengineering which led to the development of
51 synthetic ECMs (sECMs). These tunable materials are predominantly composed of biopolymers such as
52 poly (lactic acid) (PLA), poly (glycolic acid) (PGA), poly (lactic co-glycolic acid) (PLGA) and Poly (ethylene
53 glycol) (PEG), which can be functionalized with bioactive substances such as peptides, growth factors or
54 enzymes[8,9,10,]. The possible modulation of sECM's composition and chemistry offers precise control over
55 their mechanical properties, degradability, and temporal release of instructive molecules towards
56 improved tissue repair. Despite holding great promises, yet their structure and function remain simplified
57 compared to their native counterpart [11,12].
58 With the aim of combining high biological fidelity and design flexibility, engineered ECMs (eECMs) have
59 become a credible alternative. Those result from the exploitation of stem/progenitor populations capable
60 of depositing ECMs under specific in vitro culture conditions[13,14,15,16], which can be subsequently isolated
61 from the cellular fraction and exploited as a cell-laid product. Early studies were conducted using eECM
62 derived from primary cells, exhibiting variable performance associated with the inter-donor variability[17,18].

63 Most recently, we demonstrated the possibility to standardize the production of eECMs through the
64 engineering of dedicated human mesenchymal stromal/stem cell (hMSC) lines[19]. Precisely, the
65 Mesenchymal Sword of Damocles – BMP2 (MSOD-B) line offered the generation of eECMs in the form of
66 human cartilage templates[20]. Those cartilage templates can be further devitalized, lyophilized, and stored
67 as an *off-the-shelf* tissue, retaining remarkable bone formation capacity by instructing endochondral
68 ossification[21].
69 The exploitation of cell lines as an unlimited cell source for eECM generation offers unprecedented
70 standardization in graft production and performance. Meanwhile, it also consists of a robust cellular
71 platform facilitating their further genetic engineering, to achieve the production of eECMs tailored in
72 composition and function. Towards this objective, CRISPR/Cas9 appears as a versatile and efficient gene-
73 editing tool. While this technology has been extensively used for genetic screening or disease
74 modeling[22,23,24], the possibility to edit hMSCs and study the compositional impact on deposited eECMs has
75 not been investigated so far.
76 In this study, we aim at demonstrating that CRISPR/Cas9 can be applied as an editing tool for the
77 engineering of custom eECMs. As proof-of-principle, our strategy relies on the CRISPR/Cas9-guided editing
78 of the MSOD-B line for knocking out Vascular endothelial growth factor (VEGF) and Runt related
79 transcription factor 2 (RUNX2), respectively a key pro-angiogenic protein and transcription factor critically
80 involved in the endochondral ossification pathway. The resulting hMSC lines will be evaluated for their
81 capacity to generate hypertrophic cartilage in vitro and instruct tailored skeletal tissue formation in vivo
82 as cell-free and lyophilized templates. If successful, our study is expected to validate the use of
83 CRISPR/Cas9 for eECMs edited in composition, while providing a novel platform towards decoding the
84 necessary molecular signals driving effective tissue repair.
85

86 **Results**

87 **CRISPR/Cas9 editing of hMSC lines lead to efficient VEGF knockout in cartilage tissues.**

88 VEGF is a known master regulator of angiogenesis[25] and a key mediator of endochondral ossification.
89 When reaching hypertrophy, chondrocytes highly express VEGF, prompting vasculature invasion and
90 subsequent osteoprogenitor recruitment. This was proven to be essential for cartilage template
91 remodeling into bone and bone marrow[26]. However, whether VEGF is a requirement to instruct ectopic
92 endochondral ossification remains to be investigated. Here, we thus first aimed at engineering a hMSC
93 line CRISPR/Cas9-edited for VEGF knockout and evaluate the corresponding impact on cartilage and

94 endochondral bone formation (Figure 1A). To this end, we exploited the mesenchymal sword of Damocles
95 bone morphogenetic type-2 (MSOD-B) as human cell line previously demonstrated as capable of
96 endochondral ossification[20] (Supplementary Figure 1A). Specific guide RNAs (gRNAs) targeting different
97 regions of the VEGF gene but conserved across all isoforms of VEGF were designed based on a previously
98 established protocol[27] towards modifying the MSOD-B line. Three gRNAs targeting exon 1 (VEGF_1.1,
99 VEGF_1,2, VEGF1.3), one targeting exon 2 (VEGF_2.1), and one targeting exon 8 (VEGF_8.1) were designed
100 (Figure 1B, Supplementary Figure 1B). These gRNAs were cloned into the pU6-(BbsI)_CBh-Cas9-T2A-
101 mCherry vector encoding the Streptococcus pyogenes Cas9 (SpCas9) machinery. Following transfection in
102 MSOD-B cells, single cell clones were sorted based on the transient mCherry expression and expanded for
103 characterization (Figure 1A). Out of 163 single clones, 14 could be successfully expanded (8.5 %). From
104 these clones, five were retrieved from the gRNA 1.1, six from gRNA 1.3 and three from gRNA 8.1. In order
105 to assess a successful editing and directly correlate it to a knockout of VEGF, an ELISA assay was performed
106 to measure the concentration of VEGF in the supernatant of expanded MSOD-B clones (Figure 1C). In non-
107 edited cells (MSOD-B, control), 5000 pg/mL were secreted and detected by ELISA. From the successfully
108 expanded clones, most of them showed reduced but non-abolished secretion of VEGF. However, two
109 clones exhibited undetectable levels of VEGF, both resulting from the gRNA targeting the Exon1 of the
110 VEGF gene. These clones were defined as MSOD-BΔV1 and MSOD-BΔV2 and further characterized for
111 their capacity to form cartilage.

112 To this end, clones were expanded and seeded on collagen scaffold and induced for three weeks towards
113 chondrogenic differentiation followed by lyophilization of the tissues. As anticipated with the MSOD-B
114 tissues, histological assessment revealed the formation of a collagenous matrix with cartilage features
115 (Safranin-O, Figure 1D). Similarly, a successful chondrogenic differentiation and deposition of
116 glycosaminoglycans could be observed in the MSOD-BΔV1 (Figure 1D) constructs. A quantitative
117 assessment (blyscan assay) confirmed the content in glycosaminoglycans in MSOD-B and VEGF-edited
118 clones falling in the same concentration range although a lower amount was detected in the latest group
119 (Figure 1E). Importantly, VEGF quantification in corresponding pellets validated the successful knockout
120 of the protein, barely detectable in the MSOD-BΔV1 and ΔV2 tissues (47.64 pg/pellet in edited clones
121 versus 552.7 pg/pellet in MSOD-B, Figure 1F).

122 To further examine the potential impact of VEGF-editing on tissue formation, we performed
123 immunostaining analysis of the engineered cartilages. Confocal microscopy revealed strong deposition of
124 Collagen Type I (COL1) and Collagen Type X (COLX) in all samples, characteristic of mature hypertrophic

125 cartilage tissues (Figure 1G). However, while the immunostaining revealed the VEGF deposition in the
126 MSOD-B ECM, the protein could not be detected in the MSOD-BΔV1 samples (Figure 1G).

127 Taken together, this data indicates the successful generation of MSOD-B lines knocked-out in VEGF. The
128 MSOD-BΔV1 clones exhibited cartilage formation capacity with minimal level of VEGF. This validates the
129 use of CRISPR/Cas9 as a precision tool to edit the composition of cartilage tissue.

130

131 **VEGF knockout cartilage tissues retain bone remodeling capacity despite reduced early-stage**
132 **vascularization.**

133 To evaluate the functional impact of VEGF knockout in engineered constructs, we assessed both the
134 angiogenic and bone formation assays. Since the two clones exhibited similar in vitro tissue formation
135 capacity, only the MSOD-BΔV1 was selected for further performance assessment.

136 We first performed the Chorioallantoic Membrane (CAM) assay as ex vivo assessment of angiogenic
137 potential (Figure 2A). This assay provides insights into the biological activity and neovascularization
138 potential of each construct, through quantitative evaluation of vascular density around engineered grafts
139 After 4 days, we observed an extensive vessel formation in the periphery of both MSOD-B and MSOD-
140 BΔV1 lyophilized eECMs (Figure 2B). Quantification of vascular densities [30] suggested a reduced vessel
141 formation in MSOD-BΔV1 samples but without reaching significance (Figure 2C and Supplementary Figure
142 2A). Thus, the CAM assay indicated that both MSOD-B and MSOD-BΔV1 cartilages retain angiogenic
143 potentials.

144 We next investigated in vivo the impact of the VEGF knockout on the graft capacity to undergo
145 endochondral ossification, by implanting cartilage grafts subcutaneously in an immunodeficient mouse
146 model. Importantly, prior to implantation, tissues were lyophilized using a pre-established protocol[31]. This
147 allowed us to assess the performance of the generated tissue itself, in line with the idea of developing off-
148 the-shelf substitutes. Samples were extracted after two and six weeks as early and late development
149 timepoints (Figure 2D). After two weeks in vivo, we first evaluated the angiogenic potential of tissues by
150 quantitative confocal microscopy imaging of 100 µm thick sections stained for CD31, a well-defined
151 vascular marker. This allowed us to evidence a dense vascular network in MSOD-B constructs, covering
152 the entirety of the grafts (Figure 2E). Instead, MSOD-BΔV1 displayed a more limited vascularization, pre-
153 dominantly at the tissue periphery (Figure 2E). Quantification confirmed these observations with MSOD-

154 B exhibiting a significantly higher volume of vessels per total section volume (0.523 μm^3 versus 0.231 μm^3
155 for MSOD-B and MSOD-BΔV1 respectively, Figure 2F).

156 Using microtomography, we further assessed the amount of mineralized tissue formed in a temporal
157 fashion. At two weeks, the formation of a cortical ring could already be observed in both MSOD-B and
158 MSOD-BΔV1 tissues (Figure 2G). Quantifications revealed a similar bone/mineralized volume normalized
159 to the total volume of the graft (BV/TV, Figure 2H, supplementary figure 2B and 2C) with 17 % and 16 %
160 in MSOD-B and MSOD-BΔV1 samples respectively. At the six-week timepoint, trabecular structures could
161 be observed in reconstructed 3D scans from both groups (Figure 2G). Remarkably, histological analysis
162 confirmed the similar development of the tissues with bone formation (Masson´s trichrome) already at
163 two weeks post-implantation and minimal remnants of cartilage (Safranin O) (Figure 2I). At six weeks both
164 samples remodeled into fully mature bone organs, characterized by presence of cortical and trabecular
165 structures as well as a bone marrow tissue filling the cavity (Figure 2I).

166 These results indicate that the absence of VEGF in cartilage tissue can delay the early vascularization of
167 MSOD-BΔV samples. However, this did not prevent nor impact the remodeling of the lyophilized grafts
168 into bone and bone marrow tissues indicating that VEGF is non-essential in order to efficiently instruct
169 endochondral ossification.

170

171 **RUNX2 knockdown does not prevent chondrogenic differentiation but impairs hypertrophy.**

172 We next investigated whether the composition and thus function of a graft could be modified by editing
173 transcriptional factors involved in mesenchymal cell differentiation. Using CRISPR/Cas9, we thus targeted
174 the RUNX2, a known master regulator particularly important for chondrocyte differentiation and
175 hypertrophy[32,33]. We designed gRNAs targeting the coding regions involved in cell signaling integration,
176 activation, and inhibition domain which are conserved in both isoforms of RUNX2 (Figure 3A,
177 Supplementary Figure 3A).

178 One gRNA was designed for targeting exon 2 (RUNX2_2.1), one targeting exon 5 (RUNX2_5.1), two
179 targeting exon 6 (RUNX2_6.1 and RUNX2_6.2) and one targeting exon 8 (RUNX2_8.1). Similar to the VEGF
180 set-up, gRNAs were transfected in MSOD-B cells together with a pU6-(BbsI)_CBh-Cas9-T2A-mCherry
181 plasmid to ensure transfection efficiency and single cell sorting of positive clones. Out of 385 single clones,
182 62 could be successfully expanded, corresponding to a 16.1% efficiency. From these clones, five were
183 derived from the RUNX2_5.1 gRNA, 18 from RUNX2_6.1, 15 from RUNX26.2 and 24 from RUNX2_8.1.

184 To identify successfully edited clones, we first screened for those exhibiting a decrease in their RUNX2
185 protein expression using intra cellular flow cytometry. Among the 62 clones, 17 displayed a reduced
186 RUNX2 pattern as compared to the MSOD-B control (Figure 3B and Supplementary Figure 3B) and were
187 further sent for sequencing analysis. This led to the identification of two successfully edited clones,
188 demonstrating a point mutation in the exon 6 of RUNX2 gene (Supplementary Figure 3C). To confirm the
189 knockout impact on the transcription factor structure, a Western Blot analysis was conducted on cellular
190 extracts of in vitro cultured cells. MSOD-B cells exhibited intact RUNX2 proteins of 52 – 62 kDa[34,35](Figure
191 3C). Instead, the RUNX2-edited cells displayed truncated versions of 32 – 42 kDa, consistent with the
192 expected mRNA shortening.

193 These two clones were defined as MSOD-BΔR1 and MSOD-BΔR2 and further assessed for their ability to
194 form cartilage in vitro. Following 3D chondrogenic differentiation, samples were lyophilized and processed
195 for histological analysis. The presence of cartilage structures embedded in a collagenous matrix could be
196 observed in all MSOD-B, MSOD-BΔR2 (Figure 3D) and MSOD-BΔR1 tissues (Supplementary Figure 3D). This
197 was confirmed quantitatively using the Blyscan assay, with detectable glycosaminoglycans in all groups
198 (Figure 3E, Supplementary Figure 3E). Using immunostaining combined with quantitative confocal
199 microscopy, the possible impact of RUNX2-editing on tissue hypertrophy was further investigated. First,
200 Collagen Type II (COL2) staining confirmed the distribution of cartilage matrix across MSOD-B, MSOD-
201 BΔR1 and MSOD-BΔR2 samples (Figure 3F and Supplementary Figure 3F). However, we observed a clear
202 distinction in the Collagen Type X (COLX) expression pattern, a specific marker of hypertrophy which was
203 hardly detectable in MSOD-BΔR tissues (Figure 3F and Supplementary Figure 3F). Subsequent
204 quantification confirmed a significant reduction of COLX volume in MSOD-BΔR1 (0.236 μm^3) and MSOD-
205 BΔR2 (0.182 μm^3) compared to MSOD-B (0.81 μm^3) (Figure 3G, Figure 3H, Supplementary figure 3G-H-I).

206 To further characterize the functional impact of the RUNX2 knock-down, the MSOD-B and MSOD-BΔR1
207 osteogenic differentiation capacity was assessed in vitro. After 3 weeks of culture in osteogenic medium
208 (or expansion medium, control), Alizarin Red staining revealed a s a marked absence of mineralization in
209 MSOD-BΔR1 culture, while in stark contrast with MSOD-B cells (Figure 3I). Quantitative PCR analysis
210 indicated a lower expression of COLX and ALPL in MSOD-BΔR1 (Figure 3J), key osteogenic-associated
211 genes, of interest, the expression level of RUNX2 was only partially decreased in MSOD-BΔR1, in line with
212 the truncated mRNA reducing but not abrogating qPCR primers binding probability.

213 In summary, we here report the successful RUNX2 knockout in MSOD-B lines using CRISPR/Cas9. RUNX2
214 did not impair chondrogenesis but prevented the tissue hypertrophy, as well as the osteogenic potential
215 of the cells.

216

217 **RUNX2 knockout in cartilage tissues disrupts effective ectopic bone formation.**

218 To assess the corresponding impact of RUNX2-edited cartilages on bone formation, MSOD-B tissues (as
219 control) and MSOD-BΔR1 were lyophilized and implanted subcutaneously in immunodeficient mice for
220 two to six weeks. From microtomography image reconstructions, we observed an evident reduction of
221 mineralization in MSOD-BΔR1 and compared to MSOD-B (Figure 4A) already after two weeks. This
222 qualitative and visual difference in mineralization persisted after six weeks in vivo (Figure 4A). Subsequent
223 quantifications confirmed these observations with a clear reduction in BV/TV as early as week 2 (16.46 %
224 in MSOD-B and 7.01 % in MSOD-BΔR1) and persisting at week 6 (20.03% in MSOD-B and 4.25 % in MSOD-
225 BΔR1) (Figure 4B, Supplementary Figure 4A, Supplementary Figure 4B). Histological analysis revealed an
226 early bone formation at two weeks in both samples, but to a lower extent in the MSOD-BΔR1 group (Figure
227 4C). As anticipated, MSOD-B tissues underwent full remodeling after six weeks in vivo. In sharp contrast,
228 the MSOD-BΔR1 only displayed a partial maturation with limited presence of bone and bone marrow.

229 Altogether, this indicates an incomplete remodeling of RUNX2 edited samples with significantly delayed
230 cortical and trabecular structure formation. This correlates with the impaired hypertrophic phenotype in
231 the corresponding in vitro samples.

232 We next investigated a potential batch-to-batch variability in the generation of engineered cartilage
233 tissues using the various MSOD-B lines. For each modified lines, independent batches were generated and
234 the amount of glycosaminoglycans was assessed in resulting lyophilized tissues. This revealed a rather
235 consistent generation of cartilage across batches, with no statistical differences across groups
236 (Supplementary Figure 5A, Supplementary Figure 5B, Supplementary Figure 5C). We further conducted a
237 quantitative assessment of pellet volume variability across tissues (Supplementary Figure 5D), showing
238 minimal differences between the groups, indicating a limited size variation across the samples. Taken
239 together, this points at a low variability across batches of cartilage grafts displaying comparable volume
240 and GAG content.

241

242 **RUNX2 knockout in cartilage tissues leads to better cartilage regeneration in a rat osteochondral defect.**

243 In order to assess the performance of CRISPR-Cas9 edited eECMs in a relevant skeletal regenerative
244 context, a proof-of-concept study in an immunocompetent rat osteochondral defect was performed. In
245 addition to the lyophilization process, the MSOD-B and MSOD-BΔR1 tissues were also decellularized
246 following a pre-established protocol[37] in order to reduce inflammation resulting from the rat immune
247 system. We performed a quantitative assessment of the total GAG content in decellularized MSOD-B and
248 MSOD-BΔR1 constructs, showing partial preservation of GAG in the two groups compared to their living
249 counterparts (Supplementary Figure 6A). We further assessed the total DNA content in MSOD-B and
250 MSOD-BΔR1 constructs before and after decellularization as a measure of decellularization efficiency
251 (supplementary figure 6B). Post-decellularization, the DNA content was significantly reduced to around
252 540 ng/pellet for Runx2-modified constructs and 280 ng/pellet for MSOD-B grafts (supplementary figure
253 6B), accounting for a reduction of 98.1% and 97.8% in DNA content respectively indicating an efficient
254 decellularization process across samples. The tissues were subsequently placed in the sub-chondral defect
255 in the rat distal femur. The defect consisted in a drill hole of 1mm diameter and 2mm depth (Figure 5A
256 and supplementary figure 6C). Positive controls consisted of untreated healthy rats.

257 Following explantation, histological stainings and micro-tomography were performed on all sample
258 groups. Hematoxylin and Eosin (H&E) and Masson's Trichrome indicated de novo bone formation in the
259 defect area for both the MSOD-B and MSOD-BΔR1 groups (Figure 5B and supplementary figure 6D). The
260 presence of fibrotic tissue as well as a reduced marrow compartment suggested an incomplete
261 remodeling at that timepoint (Figure 5B). Upon Tartrate-resistant acid phosphatase (TRAP) staining, we
262 observed elevated osteoclastic activitiy in MSOD-B samples compared to MSOD-BΔR1 potentially
263 indicating a reduced rate of active bone formation in MSOD-BΔR1 (Figure 5C). The micro-CT quantification
264 revealed a 30% repair of the damaged bone in the defect for both MSOD-B and MSOD-BΔR1 groups (Figure
265 5D, Supplementary figure 6E). Of interest, a significantly higher trabecular separation was observed in
266 MSOD-B and MSOD-BΔR1, confirming an ongoing bone remodeling process (Figure 5E). Using the Image
267 J software, we quantified the trabecular thickness (tb.Th) in MSOD-B and MSOD-BΔR1 constructs. The
268 analysis revealed no significant differences in tb.Th between the groups, indicating that trabecular
269 architecture remained consistent across the samples (supplementary figure 6F).

270 While no statistical differences in bone formation could be identified between the two groups, the MSOD-
271 BΔR1 tissue led to a detectable regeneration of the cartilage area, as revealed by Safranin-O staining
272 (Figure 5F) in the chondral zone (Figure 5F, a,b and c magnification). Interestingly, the MSOD-BΔR1 group

273 exhibited a higher remnants of GAGs in the subchondral area and better integration (Figure 5F, d,e,f
274 magnification) to the host tissue. Quantification of cartilage tissue within condyle surface area confirmed
275 a poor-to-no repair in the MSOD-B group (1.05%, Figure 5G). In sharp contrast, the MSOD-BΔR1 implanted
276 eECMs initiated a chondral regeneration reaching approximately 20.67% of the total healthy cartilage
277 area. The integration and regeneration potential of engineered constructs was further evaluated by
278 performing a semi-quantitative histological assessment following a pre-existing grading system[39] (Table 1
279 and Supplementary table 1). This approach allows for the systematic evaluation of critical repair tissue
280 parameters, offering a comparative measure of the regenerative efficacy of the engineered constructs
281 against healthy tissue benchmarks. In the assessment of stained femur condyle sections, cellular
282 morphology and matrix staining of the MSOD-BΔR1 group (66% and 50%, respectively) were significantly
283 better compared to the MSOD-B one (33% and 16%, respectively). Although both constructs exhibited
284 reduced cartilage thickness and subchondral bone regeneration, MSOD-BΔR1 consistently outperformed
285 the MSOD-B grafts (33.33% versus 8.33% and 25% versus 16.66%). Surface regularity and integration
286 (Figure 5F) with adjacent cartilage also revealed better outcomes in MSOD-BΔR1 (41% and 50%) as
287 opposed to MSOD-B (50% and 33%), further indicating an enhanced regenerative potential of the MSOD-
288 BΔR1 constructs.

289 In conclusion, while both grafts yielded comparable bone regeneration within the osteochondral defects,
290 only the RUNX2-deleted grafts supported a cartilage regeneration.

291

292 **Discussion**

293 We here report the possibility to edit the composition and function of eECM by CRISPR/Cas9 engineering
294 of human mesenchymal lines. VEGF knockout led to successful in vitro formation of cartilage with targeted
295 protein depletion. Upon implantation, this impacted the graft vascularization onset but not the
296 endogenous instruction of the endochondral program. In turn, RUNX2 knockout prevented cartilage
297 hypertrophy in vitro, significantly delaying ectopic bone and bone marrow formation in vivo. This strategy
298 was validated in a functional osteochondral defect model, whereby prevention of cartilage hypertrophy
299 by RUNX2 deletion improved cartilage regeneration.
300 A clear interdependency of angiogenesis and osteogenesis occurs upon bone formation[40,41]. For this
301 reason, VEGF-enrichment has been naturally proposed as a strategy to accelerate or increase bone graft
302 vascularization[42,43]. Our study demonstrates that VEGF knocked-out cartilage templates retained full

303 osteoinductive potential in a challenging ectopic environment. Those results are in sharp contrast with
304 intramembranous strategies[44,45], including our previous work[19], whereby grafts remain insufficient in
305 promoting complete bone remodeling even upon VEGF-enrichment. This suggests that the first stage of
306 host progenitor recruitment by our eECM is not VEGF dependent, although subsequent tissue
307 vascularization and remodeling may be orchestrated in a second step by endogenous cell secretion. Other
308 pro-angiogenic proteins embedded in the matrix may also have compensated for the lack of VEGF, such
309 as BMP-2[20] known to stimulate endothelial cell proliferation, migration, and differentiation[46,47].
310 Conversely, RUNX2 deletion was shown to fully prevent cartilage hypertrophy, in line with published
311 mouse models also reporting a lack of endochondral ossification and lethality at birth upon RUNX2
312 knockout[48,49]. Here, MSOD-BΔR cartilage templates still exhibited osteoinductive capacity, but with
313 cortical and trabecular structures largely reduced as compared to controls. Future work may clarify if this
314 strictly results from the absence of COLX, or if an additional specific cartilage matrix component (e.g.
315 matrix metalloproteinases) impaired the instruction of endochondral ossification.
316 The performance in a regenerative context was further evaluated in an immunocompetent rat
317 osteochondral defect model[50]. We defined an early timepoint of 3-week as providing the opportunity to
318 assess the early contribution of the grafts to both the cartilage and bone tissue regeneration. Strikingly,
319 only the MSOD-BΔR could contribute to neo-chondrogenesis. We hypothesize that the absence of
320 hypertrophic features prevented the template degradation and favored its integration to native cartilage
321 Despite the repair performance being limited to an approximate 20% of native cartilage restoration, this
322 is remarkable in light of the BMP-2 content in our ECM prompting endochondral ossification [51,52,53]. In fact,
323 preventing the in vivo remodeling of engineered cartilage templates remains challenging in the skeletal
324 regeneration field, with bone marrow MSCs (BM-MSCs) cartilage systematically reaching hypertrophy and
325 subsequent ossification. The molecular mechanisms remain nonetheless elusive, warranting further
326 studies comprising additional timepoints to decipher the repair dynamic as well as the long-term stability
327 of newly formed tissue. It also prompts a comparison with other recently proposed *off-the-shelf*
328 strategies, based on ECM[54] or synthetic scaffold materials[55], in order to comprehend the feasibility to
329 exploit our grafts for stable cartilage / joint repair[56,57]. Taken together, while the relevance of CRISPR/Cas9
330 eECMs in cartilage repair remains to be further validated, our study demonstrates the relevance of
331 genetically-edited ECMs in regenerative contexts.

332 CRISPR/Cas9 editing of human mesenchymal cells has previously been explored for gene and cell therapy
333 applications[58,59] , for tailoring the immunomodulatory and/or differentiation capacity of engineered cells.
334 However, no studies have described the exploitation of editing strategies for the generation of eECMs,

335 whereby modified cells are absent from the final grafting product. Our work illustrates that this can be
336 achieved by direct targeting of secreted factors typically embedded upon ECM deposition, as
337 demonstrated with VEGF. Alternatively, we also propose the knockout of key transcription factors as a
338 strategy for custom eECM generation by impacting their tissue developmental/maturation stages.
339 A clear implication of our work lies in the possibility to decipher the necessary factors capable of
340 instructing de novo tissue formation. Those findings will be of high relevance for the design of eECMs
341 tailored in composition. Beyond bone repair, our study also bears high relevance in other regenerative
342 contexts. In fact, an exciting opportunity also lies in harnessing CRISPR/Cas9 for editing eECMs and tuned
343 their immunogenicity. Key inflammatory components could be turned down, leading to improved efficacy
344 of repair in line with the immuno-engineering principles[60,61] .
345 Importantly, our study describes the exploitation of eECMs in a lyophilized form, thus conferring an off-
346 the-shelf storage solution. While the lyophilization and decellularization process can affect the ECM
347 integrity, the resulting grafting products were demonstrated to retain regenerative properties. Together
348 with the standardization of production conferred by stable cell sources, our concept offers exciting
349 translational opportunities. In fact, instrumental to this work is the use of dedicated hMSC lines. The
350 genetic modification of primary cells is laborious, and their limited lifespan ex vivo challenges their
351 selection, characterization, and exploitation for tissue engineering applications[62,63]. Here, the MSOD-B
352 was harnessed as an unlimited cell source with robust differentiation potential. This confers a higher
353 standardization potential, although cell line-derived product can also be subject to batch dependency.
354 Our study reports a limited batch-to-batch variation but a stringent characterization of cell lines capacity
355 may be required upon substantial passage. The editing of eECMs remains tedious in part due to the limited
356 CRISPR/Cas9 efficiency and potential off-target effects, calling for a systematic clonal selection. In
357 addition, while large CRISPR/Cas9 screening can be performed in other stem cell systems[64,65], the critical
358 cell mass required for effective cartilage formation affects parallelization and leads to limited throughput.
359 Nonetheless, after the identification and characterization process, the resulting cell lines can be banked
360 and used for unlimited tissue manufacturing.
361 The MSOD-B line remains the only human cell source capable of priming endochondral ossification by
362 engineering living or cell-free grafts. This was demonstrated to be driven by the combined low dose of
363 BMP-2 embedded in the tissue (~40 ng/tissue) together with glycosaminoglycans and other thousands of
364 identified ECM proteins[20]. The BMP-2 amount is thus far below the typical amount used in sECMs
365 approaches for effective osteoinduction, falling in the microgram to milligram range[31]. This is one key
366 advantage of eECM graft, exhibiting a biological complexity that so far has not been matched by sECMs.

367 Ideally, the two approaches are complementary as the editing of eECMs could inform on the necessary
368 but sufficient factors driving effective regeneration. Those would in turn be embedded in a sECMs strategy
369 and offer a fast and possibly cost-effective solution.

370 To conclude, the present work offers a platform for decoding factors involved in tissue regeneration and
371 generate tailored eECM. Here illustrated in the context of skeletal repair, our study may offer similar
372 opportunities in other regenerative situations.

373

374 **Materials and Methods:**

375 **Cell expansion**

376 MSOD-B cells and their modified progeny were cultured in a humidified incubator at 37 °C and 5% CO_2
377 using complete medium consisting of α-minimum essential medium (αMEM) supplemented with 10%
378 fetal bovine serum, 1% HEPES, 1% sodium pyruvate, 1% penicillin-streptomycin-glutamine solution, and 5
379 ng/ml of fibroblast growth factor-2 (FGF-2) (all from Gibco). Cells were seeded at a density of 3200
380 cells/cm^2 until they reached 90% confluency. The medium was replaced twice a week.

381 **Chondrogenic and osteogenic differentiation**

382 MSOD-B cells and their modified progeny were harvested from culture flasks by adding Trypsin-EDTA
383 (0.25%) (Gibco) and subsequently seeded on cylindrical Collagen Type I scaffold (Avitene™ Ultrafoam™
384 Collagen Sponge, Davol) of 6 mm in diameter and 3 mm in thickness at a density of 2 x 10^6 cells per scaffold
385 in 12 well plates coated with 1 % agarose (Sigma) for chondrogenic differentiation and in a 12-well plate
386 for osteogenic differentiation. Tissue constructs were cultured for three weeks in chondrogenic medium
387 (DMEM supplemented with 1% penicillin-streptomycin-glutamine, 1% HEPES (1M), 1% sodium pyruvate
388 (100 mM), 1% ITS (100x) (Insulin, Transferrin, Selenium) (all from Gibco), 0,47 mg/ml linoleic acid (Sigma),
389 0.12% bovine serum albumin (25 mg/mL) (BSA) (Sigma), 0.1 mM ascorbic acid (Sigma), 10^{-7} M
390 dexamethasone (Sigma) and 10 ng/ml TGF-β3 (Novartis)). The cells in the 12 well plates were
391 supplemented for three weeks with osteogenic (or expansion medium, control) differentiation medium
392 (α-minimum essential medium (αMEM) with 10% fetal bovine serum, 1% HEPES (1M), 1% sodium pyruvate
393 (100 x 10^{-3}M) and 1% penicillin-streptomycin-glutamine solution (100X), supplemented with 0.01M β-
394 dexamethasone and 0.1M ascorbic acid). Media were replaced twice a week.

395 **Lyophilization**

396 After three weeks of chondrogenic differentiation, the tissue constructs were rinsed twice with PBS 7.2
397 (without calcium/magnesium Gibco), snap frozen in liquid nitrogen for five minutes and then lyophilized
398 using a freeze dryer (Labconco) (-80 °C and 0.05 mbar) overnight. Thereafter, the lyophilized tissue
399 constructs were stored at 4 °C.

400 **Decellularization**

401 After lyophilization, the tissue constructs were treated with a solution containing 1% SDS (Sigma-Aldrich)
402 and DNase I (Sigma-Aldrich) to remove cellular material as according to Elder et al., Biomaterials 2009.
403 The constructs were then thoroughly rinsed with PBS (7.2, without calcium/magnesium; Gibco) to
404 eliminate residual chemicals. Following the washing step, the scaffolds were snap-frozen in liquid nitrogen
405 for five minutes and re-lyophilized using a freeze dryer (Labconco) at -80°C and 0.05 mbar overnight. The
406 resulting decellularized tissues were stored at 4°C until experimental use.

407 **Transfection of MSOD-B cells with gRNAs**

408 MSOD-B cells were seeded at a density of 400,000 cells per well in 12 well plates to reach a minimum of
409 80% confluency the following day. The medium was replaced before transfection. The transfection was
410 performed with a / ratio of 2 µL lipofectamine to 1 µg DNA. A DNA mix was prepared for each of the five
411 gRNAs and the two plasmid controls. DNA mixtures were composed of 1 µg of plasmid, 2 µL of P3000
412 reagent and 50 µL of OptiMEM (Thermo-Fischer). A lipofectamine cocktail was prepared for all DNA
413 mixtures consisting of 24 µL of lipofectamine 3000 in 400 µL of OptiMEM. Lipofectamine and the DNA
414 mixtures were added at a 1:1 ratio. After 48h, cells were analyzed and mCherry positive clones were FACS
415 sorted as single cells in 96-well plates using ARIAIII (BD Biosciences). Successfully expanded clones were
416 then further characterized.

417 **ELISA**

418 VEGF protein content was measured in supernatant collected from cells seeded at 570 cells/cm^2 in T175
419 flask and cultured for 3 days. Content from engineered cartilage tissues was assessed following digestion
420 in RIPA buffer. The Quantikine ELISA kit for Human VEGF-A Immunoassay from the R&D System was used
421 according to the manufacturer instructions to determine protein concentration.

422 **Intracellular flow cytometry**

423 MSOD-B and MSOD-B ΔRUNX2 cells were trypsinized, fixed and permeabilized using the
424 Fixation/Permeabilization Kit (BD Biosciences). Following a blocking step in 10% normal donkey serum

425 (Sigma), cells were stained with a primary antibody against RUNX2 (Rabbit anti-human, Thermo-Fischer
426 PA5-82787) for one hour at room temperature. After primary antibody incubation, cells were washed and
427 stained with an Allophycocyanin (APC) labeled secondary antibody (Donkey anti-rabbit IgG DyLight™ 649,
428 Biolegend 406406) for 30-45 minutes at room temperature in 2% normal donkey serum. The Control
429 samples consisted of unstained cells (negative control) and cells incubated only with the secondary
430 antibody (secondary Ab control). Data were recorded on a BD LSRFortessa™ Cell Analyzer (BD
431 Biosciences). FCS files were analyzed using the FlowJo™ software (FlowJo LLC, 10.5.3, BD Biosciences).

432 **Western blotting**

433 MSOD-B and MSOD-B ΔRUNX2 cells were trypsinized and washed with ice cold PBS twice and lysed on ice
434 for 10 min in RIPA buffer (#10017003, Thermo Fisher Scientific) supplemented with 1× proteinase and
435 phosphatase inhibitor cocktail (#78440, Thermo Fisher Scientific). The lysates were centrifuged at 16,
436 000*g* for 15 min +4 °C, and the supernatants were collected. Sample buffer (Laemmli buffer (#161-0737,
437 BioRad) supplemented with 5% 2-mercaptoethanol, 1× proteinase and phosphatase inhibitor cocktail
438 (#78440, Thermo Fisher Scientific) was added to the supernatant at 1:1 ratio. Samples were boiled at 95
439 °C for 5 minutes and stored at −80 °C or kept on ice until gel loading. Proteins were separated using Bolt
440 gels according to manufacturer's protocol (#NW04122, #B0002, Thermo Fisher Scientific). iBlot2 system
441 was used to transfer the proteins on polyvinylidene fluoride membrane (PVDF) membrane according to
442 manufacturer's protocol (#IB24001, Thermo Fisher Scientific). PVDF membrane was washed once in 1×
443 PBST buffer (#28352, Thermo Fisher Scientific) and blocked in 2% blocking solution (#10156414, Thermo
444 Fisher Scientific) for 1 h at room temperature. Membranes were incubated overnight at +4 °C with primary
445 antibodies at recommended concentrations in 1% blocking solution. Membranes were washed three
446 times (5 min for each wash) with 1× PBST buffer, and secondary HRP-conjugated antibodies in 1% blocking
447 solution were added to the membranes at 1:5000 concentration for 1 h incubation at room temperature.
448 Membranes were washed three times with 1× PBST and proteins were detected by chemiluminescence
449 according to manufacturer's protocol (#RPN2232, Thermo Fisher Scientific). The following antibodies
450 were used. primary antibodies: RunX– (D1L7F - 12556) from Cell Signaling Technology and Actin (612656)
451 is from Becton Dickinson. The secondary antibodies were anti-Mouse (GENA931) from Sigma-Aldrich, anti-
452 Rabbit (NA9340V) from Thermo Fisher Scientific.

453 **Biochemical analysis**

454 Lyophilized tissue constructs were digested by overnight incubation in 0.5 ml of Proteinase K solution (1
455 mg/mL Proteinase K, Sigma; 10 ug/ml pepstatin A, Sigma; 1 mM EDTA, Sigma; 100 mM Iodoacetamide;

456 50mM Tris) at pH 7.6 and 56 °C. The GAG content of digested samples was analyzed using
457 Glycosaminoglycan Assay Blyscan kit (Biocolor) following the manufacturer instruction. DNA residues
458 were quantified using the CyQuant NF Cell Proliferation Assay Kit (Thermo-Fisher, USA) following the
459 manufacturer's instructions, with an excitation wavelength of 485 nm and an emission wavelength of 535
460 nm.

461 **Mice**

462 FoxN1 KO BALB/C (nude mice) 6–8-weeks old, were obtained from Charles River Laboratories. All mouse
463 experiments and animal care were performed in accordance with the Lund University Animal Ethical
464 Committee guidelines (ethical permit #M15485–18). Mice were housed at a 12-hour light cycle in
465 individually ventilated cages at a positive air pressure and constant temperature. Mice were fed with
466 autoclaved diet and water ad libitum. During the implantation procedure, anaesthesia was performed
467 with 2-3 % Isoflurane (Attane). The mice were kept on a heating pad during the procedure to avoid the
468 heat loss.

469 **Micro-CT scanning**

470 In vivo samples were explanted and fixed overnight with 4% formaldehyde before ex vivo micro-CT
471 analysis using a U-CT system (MILABS, Netherland) equipped with a tungsten x-ray source at 50 kV and
472 0.21 mA. Volumes were reconstituted at 10 µm isotropic voxel size. For total volume (TV) analysis, each
473 sample was assessed with Blender (v2.82a, Netherland). Briefly, a mesh was created surrounding the 3D
474 reconstruction of each sample and the volume occupied was then quantified. For bone volume (BV)
475 analysis, the highly mineralized tissue volume was quantified using Seg3D (v2.2.1, NIH, NCRR, Science
476 Computing and Imaging Institute (SCI))

477 **Sample preparation for histological analysis.**

478 In vitro samples were directly fixed prior to sectioning. In vivo samples were fixed and subsequently
479 decalcified with a 10% EDTA solution, pH = 8, at 4 °C for two weeks prior to tissue embedding.
480 Paraffin embedding was performed on samples fixed in 4% formalin (Solveca AB). Tissues were
481 dehydrated by immersion in consecutive solutions of 35%, 70%, 95%, and 99.5% graded ethanol solution
482 (Solveco AB). Immersion in a 99.5% ethanol/xylene solution (1:1, Fisher Scientific) was then performed
483 for ten minutes followed by two rinsing in xylene (Fisher Scientific) for 20 minutes. Subsequently,
484 tissues were embedded in paraffin at 56 °C overnight, before sectioning with a microtome (Microm HM
485 355 Rotary Microto–e) in 5 - 10 µm sections. The sections were then dried overnight at 37 °C before

486 staining. Prior to staining, sections were deparaffinized by two washes in xylene for 7 minutes and once
487 in 99.5% ethanol/xylene solution (1:1) for 3 minutes. Afterwards, sections were hydrated twice in
488 consecutive solutions of 99.5%, 95%, 70%, and 35% ethanol, for 7 minutes each.

489 Agarose embedding was performed on samples fixed overnight with 4% paraformaldehyde (Thermo
490 Scientific), using 4% low-melting agarose (Sigma). Sections of 100 µm thickness were obtained using a
491 7000smz vibratome (Campden) with stainless steel or ceramic blades.

492 **Safranin O Staining**

493 Paraffin-embedded sections were stained using Mayer's hematoxylin solution (Sigma-Aldrich) for 10
494 minutes. Samples were then placed under running distilled water to remove superfluous staining from
495 the sections. Subsequently, sections were stained with 0.01% fast green solution (Fisher Scientific) for five
496 minutes and rinsed with 1% acetic acid solution (glacial, Fisher Scientific) for 15 seconds. After that, the
497 slides were stained with 0.1% safranin O (Fisher Scientific) solution for 5 minutes. Dehydration and
498 clearing were performed by immersion in 95%, 99.5% ethanol, 99.5% ethanol/xylene solution (1:1) and
499 xylene twice successively for 2 minutes. Finally, the stained slides were mounted with glass slides using
500 PERTEX mounting medium (PERTEX, HistoLab).

501 **Masson's trichrome staining**

502 Masson's trichrome staining was performed using the trichrome staining kit (Sigma-Aldrich Sweden AB)
503 according to the manufacturer's guidelines. Briefly, tissue sections were deparaffinized and immersed in
504 cold running deionized water for 3 minutes. Then the sections were kept in Bouin's solution at room
505 temperature overnight or at 56 °C for 15 minutes. The slides were washed by running tap water and
506 stained using working Weigert's iron hematoxylin solution (Sigma) for five minutes for nuclei detection
507 (in black). After washing the slides, the cytoplasm was stained in red with Biebrich Scarlet-Acid fuchsin for
508 five minutes followed by clearing the slides by immersion in working phosphotungstic/ phosphomolybdic
509 acid solution for five minutes. Collagen stained blue by immersion in aniline blue solution for five minutes
510 followed by clearing in 1% acetic acid (glacial, Fisher Scientific) solution diluted in distilled water (glacial,
511 Fisher Scientific) for two minutes and washing with running deionized water. Finally, the sections were
512 dehydrated in graded ethanol solutions (95% once, 100% twice) for two minutes each before washing
513 with xylene twice for two minutes and mounted with PERTEX mounting medium.

514 **Hematoxylin and Eosin staining**

515 Paraffin-embedded sections were stained using Mayer's hematoxylin solution (Sigma-Aldrich) for 10

516 minutes. Samples were then placed under running distilled water to remove superfluous staining from
517 the sections. The slides were immersed precisely in 1X phosphate-buffered saline (PBS) for 1 minute to
518 intensify the blue nuclei staining while preserving tissue integrity. Following this, a thorough rinse with 3
519 changes of distilled water effectively removed any residual PBS, preparing the sections for the subsequent
520 counterstaining step. Subsequently, Alcoholic-Eosin (Sigma-Aldrich) was applied for 1 minute as the
521 counterstain without any rinsing post-application, ensuring optimal interaction of the staining solution
522 with the tis. Dehydration and clearing were performed by immersion in 95%, 99.5% ethanol, 99.5%
523 ethanol/xylene solution (1:1) and xylene twice successively for 2 minutes. Finally, the stained slides were
524 mounted with glass coverslips using PERTEX mounting medium (PERTEX, HistoLab).

525 **Quantitative PCR**

526 Total RNA isolation was conducted from in vitro engineered tissues utilizing the Quick-RNA extraction kit
527 (Zymo Research, R1055) following the manufacturer's protocol. Subsequently, cDNA extraction was
528 carried out using cDNA synthesis kit (Invitrogen 11917020). The quantitative real-time polymerase chain
529 reaction (qRT-PCR) was performed, utilizing the assay on demand from Applied Biosystems to assess the
530 expression of specific genes. These genes include glyceraldehyde 3-phosphate dehydrogenase (GAPDH,
531 HS02786624_G1), runt-related transcription factor 2 (Runx2, Hs00231692_m1), alkaline phosphatase
532 (ALP, Hs01029144_m1), and collagen type X (ColX, Hs00166657_m1).

533 **Rat osteochondral defect model**

534 Ten- to 12-week-old male Sprague Dawley rats (n=11) were purchased from JANVIER LABS
535 (France). After 7 days of acclimation the rats were anesthetized using 3% isoflurane. Then,
536 animals were placed on a 37°C warm heating pad in prone position. Once anesthetized, isoflurane
537 was lowered to 2 to 2.5%, and buprenorphine (Temgesic, 30 µg/kg; Indivior Europe Ltd., Dublin,
538 Ireland) was injected subcutaneously for analgesia. The right hind limb of the animal was shaved
539 and carefully disinfected, and an incision was made along the skin and soft tissue to expose the
540 right knee. After cleaning the knee laterally from soft tissue, patella was displaced laterally to
541 expose the distal femur. An articular cartilage defect with 2mm depth and 1mm diameter was
542 created at the trochlear groove of femur. The defect was then push-fitted with the grafts, and
543 not secured with any sutures. The wound was closed in a layered fashion using resorbable sutures
544 (Vicryl 45-0, Ethicon, Somerville, USA) by closing the joint capsule, followed by the muscle tissue
545 (continuous interlaced suture), followed by closing the skin (Donati suture). Animals started load

546 bearing immediately after surgery. After 3 weeks (n=11) animals were anesthetized by isoflurane
547 inhalation (3%), followed by CO2 asphyxiation, and right-femur were harvested prior to
548 subsequent micro-CT and histological characterization.

549 **Histology grading method**

550 Histological sections from rat femur condyles were stained with Safranin-O, Masson's trichrome, and H&E
551 staining. For each sample, sections were compiled at different depth (top, middle and bottom) defined to
552 encompass the full tissue characteristics. A semi-quantitative analysis of the repaired tissue was
553 performed by utilizing a customized adaptation of the histological grading system initially outlined by
554 Wakitani et al[66]. This modified scale encompasses six distinct parameters: cellular morphology, matrix
555 staining, surface regularity, cartilage thickness, regenerated subchondral bone formation, and integration
556 with neighbouring cartilage. Each parameter was graded on a numerical scale ranging from 0 to 4 points
557 by independent expert observers, where a maximum total score of 16 indicates the presence of tissue
558 displaying characteristics akin to entirely healthy and normal tissue (Table 1).

559 **Cartilage quantification method**

560 An evaluation of three distinct sites within the condyle defect was conducted to ascertain the proportion
561 of cartilage in each knee. Utilizing the measured femoral condyle thickness (200µm) and defect length
562 (1mm), a standardized Region of Interest (ROI) was defined using ImageJ. The percentage of cartilage-
563 positive regions within each defect was calculated in relation to the total ROI size, offering a quantitative
564 assessment of cartilage regeneration. This identical approach was applied to evaluate the percentage of
565 cartilage in the healthy control samples.

566 **Trabecular thickness (Tb.Th) and trabecular separation (Tb.Sp)**

567 Image analysis was performed by ImageJ. To evaluate the defect space, a rectangular interface region
568 (2 × 1 mm) was defined as the Region of Interest . Trabecular thickness (Tb.Th) and trabecular separation
569 (Tb.Sp),was calculated inside the ROI using BoneJ plugin.

570 **Chick chorioallantoic membrane (CAM) assay**

571 Fertilized eggs from Lohmann Brown chicken were commercially purchased and incubated 6 days prior
572 (Day -6) in a BINDER incubator at 37.5 °C with constant humidity. A small window in the shell was opened
573 3 days prior (Day -3) to the start of the experiment under aseptic conditions. The window was resealed
574 with adhesive tape and eggs were returned to the incubator. On day 0, MSOD-B and MSOD-BΔV1 in vitro

575 differentiated and lyophilized samples were placed on top of the CAM. Eggs were resealed and returned
576 to the incubator. Pictures were taken with a brightfield microscope (LEICA S9i) on Day 4 and analysed for
577 vascular density.

578 **Vascular density quantification**

579 To assess vascular density, the Quantitative Vascular Analysis Tool (Q-VAT)[30] was utilized. The images were
580 acquired using a digital microscope. These images were then segmented into tiles for detailed analysis.
581 The binary vascular masks were generated using the Q-VAT's automated capabilities, to distinguish
582 vascular structures within the tissue. The tool then facilitated the separation of vessel measurements
583 based on their diameters, allowing for a differentiated quantification of macro- and microvasculature.
584 These binary masks were then processed to calculate the vascular density, which refers to the proportion
585 of the tissue area occupied by vessels. This quantitative metric was evaluated for each tile, and the mean
586 vascular density was computed across all tiles for each tissue sample. As part of the analysis, we applied
587 Q-VAT to double or triple-stained slides to quantify the overlapping percentage of vessels, comparing
588 various time points to observe changes over the course of the experiment.

589 **Immunofluorescence**

590 Agarose-embedded sections were treated with 0.5% Triton X-100 (Sigma) in PBS supplemented with 20%
591 donkey serum (Jackson ImmunoResearch) for one hour at room temperature (RT) for blocking and
592 permeabilization. After blocking/permeabilization, sections were stained with primary antibodies (mouse
593 anti-Collagen II (Invitrogen, MA137493), Anti-Collagen 1 (Abcam, ab138492), VEGF polyclonal antibody
594 (Bioss Antibodies, bs-0279R), rabbit anti-Collagen Type X (ColX) (abbexa, abx101469), Goat anti
595 mouse/rat CD31 (R&D system, YZU0119121), VEGF at 4 °C overnight. Sections were washed three times
596 using cold PBS with 0.1% Triton X-100, 20 minutes each, followed by staining with secondary antibodies
597 (CF568 donkey anti-rabbit (Biotium, 20098), CF567 anti-goat (Invitrogen, A11057), CF633 donkey anti-
598 mouse (Sigma-Aldrich, SAB4600131 in 2% donkey serum for three hours at room temperature. Sections
599 were washed three times using cold PBS with 0.1% Triton X-100, 20 minutes each once more.
600 All sections were mounted using the Vectashield antifade mounting medium containing DAPI (Vector
601 Laboratories, H1200). A LSM780 confocal microscope (Zeiss) with a 10x/20x objective was used to capture
602 images and image series of whole tissue sections (z-step = 2 µm). The IMARIS 9.5 software package (Oxford
603 Instruments) was used to analyze the data.
604

605 **Acknowledgements**

606 We express our gratitude to the following facilities and individuals for their invaluable support and
607 contributions to this study: FACS Facility (Anna Hammarberg), Cell and Gene Therapy core facility (Pia
608 Johansson) and Imaging Facility at Lund Stem Cell Centre, as well as the Lund University Bioimaging
609 Centre, for providing access to the X-ray CT system. This research study was made possible by financial
610 support through the Knut and Alice Wallenberg grant, the Medical Faculty at Lund University, the Swedish
611 Research Council (Starting grant to P.E.B), the European Research Council (Starting grant hOssicle #948588
612 to P.E.B), and Region Skåne. Figures were generated using BioRender. Special thanks to Ani Grigoryan for
613 her expertise and valuable insights regarding FACS experiments. Christian Hansen deserves our
614 appreciation for providing the mcherry plasmid and offering valuable guidance and knowledge related to
615 CRISPR-Cas9.

616

617 **References**

618 1. Bonnans C, Chou J, Werb Z. Remodelling the extracellular matrix in development and disease.
619 *Nat Rev Mol Cell Biol*. 2014;15(12):786-801. doi:10.1038/nrm3904

620 2. Hussey GS, Dziki JL, Badylak SF. Extracellular matrix-based materials for regenerative medicine.
621 *Nat Rev Mater*. 2018;3(7):159-173. doi:10.1038/s41578-018-0023-x

622 3. Fattahi R, Chamkhorami FM, Taghipour N, Keshel SH. The effect of extracellular matrix
623 remodeling on material-based strategies for bone regeneration: Review article. *Tissue Cell*.
624 2022;76(January):101748. doi:10.1016/j.tice.2022.101748

625 4. Mouw JK, Ou G, Weaver VM. Extracellular matrix assembly: A multiscale deconstruction. *Nat Rev*
626 *Mol Cell Biol*. 2014;15(12):771-785. doi:10.1038/nrm3902

627 5. Assunção M, Dehghan-Baniani D, Yiu CHK, Später T, Beyer S, Blocki A. Cell-Derived Extracellular
628 Matrix for Tissue Engineering and Regenerative Medicine. *Front Bioeng Biotechnol*.
629 2020;8(December):1-10. doi:10.3389/fbioe.2020.602009

630 6. Hinderer S, Layland SL, Schenke-Layland K. ECM and ECM-like materials - Biomaterials for
631 applications in regenerative medicine and cancer therapy. *Adv Drug Deliv Rev*. 2016;97:260-269.
632 doi:10.1016/j.addr.2015.11.019

633 7. Hinderer S, Layland SL, Schenke-Layland K. ECM and ECM-like materials - Biomaterials for
634 applications in regenerative medicine and cancer therapy. *Adv Drug Deliv Rev*. 2016;97:260-269.
635 doi:10.1016/j.addr.2015.11.019

636 8. Fattahi R, Chamkhorami FM, Taghipour N, Keshel SH. The effect of extracellular matrix
637 remodeling on material-based strategies for bone regeneration: Review article. *Tissue Cell*.
638 2022;76(January):101748. doi:10.1016/j.tice.2022.101748

639 9. Tang G, Liu Z, Liu Y, et al. Recent Trends in the Development of Bone Regenerative Biomaterials.
640 *Front Cell Dev Biol*. 2021;9(May):1-18. doi:10.3389/fcell.2021.665813

641 10. Gao C, Peng S, Feng P, Shuai C. Bone biomaterials and interactions with stem cells. *Bone Res*.
642 2017;5(May):1-33. doi:10.1038/boneres.2017.59

643 11. Filippi M, Born G, Chaaban M, Scherberich A. Natural Polymeric Scaffolds in Bone Regeneration.
644 *Front Bioeng Biotechnol*. 2020;8(May). doi:10.3389/fbioe.2020.00474

645 12. Reddy MSB, Ponnamma D, Choudhary R, Sadasivuni KK. A comparative review of natural and
646 synthetic biopolymer composite scaffolds. *Polymers (Basel)*. 2021;13(7).
647 doi:10.3390/polym13071105

648 13. Decaris ML, Leach JK. Design of experiments approach to engineer cell-secreted matrices for
649 directing osteogenic differentiation. *Ann Biomed Eng*. 2011;39(4):1174-1185.
650 doi:10.1007/s10439-010-0217-x

651 14. Harvestine JN, Orbay H, Chen JY, Sahar DE, Leach JK. Cell-secreted extracellular matrix,
652 independent of cell source, promotes the osteogenic differentiation of human stromal vascular
653 fraction. *J Mater Chem B*. 2018;6(24):4104-4115. doi:10.1039/c7tb02787g

654 15. Hoch AI, Mittal V, Mitra D, Vollmer N, Zikry CA, Leach JK. Cell-secreted matrices perpetuate the
655 bone-forming phenotype of differentiated mesenchymal stem cells. *Biomaterials*. 2016;74:178-
656 187. doi:10.1016/j.biomaterials.2015.10.003

657 16. Haumer A, Bourgine PE, Occhetta P, Born G, Tasso R, Martin I. Delivery of cellular factors to
658 regulate bone healing. *Adv Drug Deliv Rev*. 2018;129:285-294. doi:10.1016/j.addr.2018.01.010

659 17. Sadr N, Pippenger BE, Scherberich A, et al. Enhancing the biological performance of synthetic
660 polymeric materials by decoration with engineered, decellularized extracellular matrix.
661 *Biomaterials*. 2012;33(20):5085-5093. doi:10.1016/j.biomaterials.2012.03.082

662 18. Prewitz MC, Seib FP, von Bonin M, et al. Tightly anchored tissue-mimetic matrices as instructive
663 stem cell microenvironments. *Nat Methods*. 2013;10(8):788-794. doi:10.1038/nmeth.2523

664 19. Bourgine PE, Gaudiello E, Pippenger B, et al. Engineered Extracellular Matrices as Biomaterials of
665 Tunable Composition and Function. *Adv Funct Mater*. Published online 2017.
666 doi:10.1002/adfm.201605486

667 20. Pigeot S, Klein T, Gullotta F, et al. Manufacturing of Human Tissues as off-the-Shelf Grafts
668 Programmed to Induce Regeneration. *Advanced Materials*. 2021;33(43).
669 doi:10.1002/adma.202103737

670 21. Grigoryan A, Zacharaki D, Balhuizen A, et al. Engineering of human mini-bones for the
671 standardized modeling of healthy hematopoiesis, leukemia and solid tumor metastasis. *bioRxiv*.
672 Published online 2021:2021.09.11.459806.
673 https://www.biorxiv.org/content/10.1101/2021.09.11.459806v1%0Ahttps://www.biorxiv.org/co
674 ntent/10.1101/2021.09.11.459806v1.abstract

675 22. Golchin A, Shams F, Karami F. Advancing Mesenchymal Stem Cell Therapy with CRISPR/Cas9 for
676 Clinical Trial Studies. In: *Cell Biology and Translational Medicine,*. Vol 8. ; 2019:89-100.
677 doi:10.1007/5584_2019_459

678 23. Hazrati A, Malekpour K, Soudi S, Hashemi SM. CRISPR/Cas9-engineered mesenchymal
679 stromal/stem cells and their extracellular vesicles: A new approach to overcoming cell therapy
680 limitations. *Biomedicine & Pharmacotherapy*. 2022;156:113943.
681 doi:10.1016/j.biopha.2022.113943

682 24. Geurts MH, Clevers H. CRISPR engineering in adult stem cell-derived organoids for gene repair
683 and disease modelling. 2023;1(January):32-45. doi:10.1038/s44222-022-00013-5

684 25. Hu K, Olsen BR. The roles of vascular endothelial growth factor in bone repair and regeneration.
685 *Bone*. 2016;91:30-38. doi:10.1016/j.bone.2016.06.013

686 26. Duda GN, Geissler S, Checa S, Tsitsilonis S, Petersen A, Schmidt-Bleek K. The decisive early phase
687 of bone regeneration. *Nat Rev Rheumatol*. 2023;19(February):78-95. doi:10.1038/s41584-022-
688 00887-0

689 27. Ran FA, Hsu PD, Wright J, Agarwala V, Scott DA, Zhang F. Genome engineering using the CRISPR-
690 Cas9 system. *Nat Protoc*. 2013;8(11):2281-2308. doi:10.1038/nprot.2013.143

691 28. joces_113_1_59.

692 29. Wang L, Wan L, Zhang T, et al. A Combined Treatment of BMP2 and Soluble VEGFR1 for the
693 Enhancement of Tendon-Bone Healing by Regulating Injury-Activated Skeletal Stem Cell Lineage.
694 *American Journal of Sports Medicine*. 2024;52(3):779-790. doi:10.1177/03635465231225244

695 30. Callewaert B, Gsell W, Himmelreich U, Jones EAV. Q-VAT: Quantitative Vascular Analysis Tool.
696 *Front Cardiovasc Med*. 2023;10. doi:10.3389/fcvm.2023.1147462

697 31. Pigeot S, Klein T, Gullotta F, et al. Manufacturing of Human Tissues as off-the-Shelf Grafts
698 Programmed to Induce Regeneration. *Advanced Materials*. 2021;33(43).
699 doi:10.1002/adma.202103737

700 32. Otto F, Thornell AP, Crompton T, et al. Cbfa1, a candidate gene for cleidocranial dysplasia
701 syndrome, is essential for osteoblast differentiation and bone development. *Cell*. 1997;89(5):765-
702 771. doi:10.1016/S0092-8674(00)80259-7

703 33. Komori T, Yagi * H., Nomura S, Yamaguchi A. Targeted disruption of. *Proc Natl Acad Sci U S A*.
704 1998;95(15):8692-8697.

705 34. Kim HJ, Kim WJ, Ryoo HM. Post-Translational Regulations of Transcriptional Activity of RUNX2.
706 *Mol Cells*. 2020;43(2):160-167. doi:10.14348/molcells.2019.0247

707 35. Hattori EY, Masuda T, Mineharu Y, et al. A RUNX-targeted gene switch-off approach modulates
708 the BIRC5/PIF1-p21 pathway and reduces glioblastoma growth in mice. *Commun Biol*.
709 2022;5(1):1-11. doi:10.1038/s42003-022-03917-5

710 36. Chen H, Ghori-Javed FY, Rashid H, et al. Runx2 regulates endochondral ossification through
711 control of chondrocyte proliferation and differentiation. *Journal of Bone and Mineral Research*.
712 2014;29(12):2653-2665. doi:10.1002/jbmr.2287

713 37. Elder BD, Eleswarapu S V., Athanasiou KA. Extraction techniques for the decellularization of
714 tissue engineered articular cartilage constructs. *Biomaterials*. 2009;30(22):3749-3756.
715 doi:10.1016/j.biomaterials.2009.03.050

716 38. Komori T. Runx2, an inducer of osteoblast and chondrocyte differentiation. *Histochem Cell Biol*.
717 2018;149(4):313-323. doi:10.1007/s00418-018-1640-6

718 39. Maehara H, Sotome S, Yoshii T, et al. Repair of large osteochondral defects in rabbits using
719 porous hydroxyapatite/collagen (HAp/Col) and fibroblast growth factor-2 (FGF-2). *Journal of*
720 *Orthopaedic Research*. 2010;28(5):677-686. doi:10.1002/jor.21032

721 40. Kusumbe AP, Ramasamy SK, Adams RH. Coupling of angiogenesis and osteogenesis by a specific
722 vessel subtype in bone. *Nature*. 2014;507(7492):323-328. doi:10.1038/nature13145

723 41. Tuckermann J, Adams RH. The endothelium–bone axis in development, homeostasis and bone
724 and joint disease. *Nat Rev Rheumatol*. 2021;17(10):608-620. doi:10.1038/s41584-021-00682-3

725 42. Largo RD, Burger MG, Harschnitz O, et al. VEGF Over-Expression by Engineered BMSC Accelerates
726 Functional Perfusion, Improving Tissue Density and In-Growth in Clinical-Size Osteogenic Grafts.
727 *Front Bioeng Biotechnol*. 2020;8(July):1-13. doi:10.3389/fbioe.2020.00755

728 43. Yang YQ, Tan YY, Wong R, Wenden A, Zhang LK, Rabie ABM. The role of vascular endothelial
729 growth factor in ossification. *Int J Oral Sci*. 2012;4(2):64-68. doi:10.1038/ijos.2012.33

730 44. Burger MG, Grosso A, Briquez PS, et al. Robust coupling of angiogenesis and osteogenesis by
731 VEGF-decorated matrices for bone regeneration. *Acta Biomater*. 2022;149:111-125.
732 doi:10.1016/j.actbio.2022.07.014

733 45. Behr B, Tang C, Germann G, Longaker MT, Quarto N. Locally applied vascular endothelial growth
734 factor A increases the osteogenic healing capacity of human adipose-derived stem cells by
735 promoting osteogenic and endothelial differentiation. *Stem Cells*. 2011;29(2):286-296.
736 doi:10.1002/stem.581

737 46. Zuo WH, Zeng P, Chen X, Lu YJ, Li A, Wu J Bin. Promotive effects of bone morphogenetic protein 2
738 on angiogenesis in hepatocarcinoma via multiple signal pathways. *Sci Rep*. 2016;6(July):1-9.
739 doi:10.1038/srep37499

740 47. Lowery JW, de Caestecker MP. BMP signaling in vascular development and disease. *Cytokine*
741 *Growth Factor Rev*. 2010;21(4):287-298. doi:10.1016/j.cytogfr.2010.06.001

742 48. Kamekura S, Kawasaki Y, Hoshi K, et al. Contribution of runt-related transcription factor 2 to the
743 pathogenesis of osteoarthritis in mice after induction of knee joint instability. *Arthritis Rheum*.
744 2006;54(8):2462-2470. doi:10.1002/art.22041

745 49. Komori T, Yagi * H., Nomura S, Yamaguchi A. Targeted disruption of. *Proc Natl Acad Sci U S A*.
746 1998;95(15):8692-8697.

747 50. Meng X, Ziadlou R, Grad S, et al. Animal Models of Osteochondral Defect for Testing Biomaterials.
748 *Biochem Res Int*. 2020;2020. doi:10.1155/2020/9659412

749 51. Sekiya I, Vuoristo JT, Larson BL, Prockop DJ. In vitro cartilage formation by human adult stem cells
750 from bone marrow stroma defines the sequence of cellular and molecular events during
751 chondrogenesis. *Proc Natl Acad Sci U S A*. 2002;99(7):4397-4402. doi:10.1073/pnas.052716199

752 52. Pelttari K, Winter A, Steck E, et al. Premature induction of hypertrophy during in vitro
753 chondrogenesis of human mesenchymal stem cells correlates with calcification and vascular
754 invasion after ectopic transplantation in SCID mice. *Arthritis Rheum*. 2006;54(10):3254-3266.
755 doi:10.1002/art.22136

756 53. Mueller MB, Tuan RS. Functional characterization of hypertrophy in chondrogenesis of human
757 mesenchymal stem cells. *Arthritis Rheum*. 2008;58(5):1377-1388. doi:10.1002/art.23370

758 54. Browe DC, Burdis R, Díaz-Payno PJ, et al. Promoting endogenous articular cartilage regeneration
759 using extracellular matrix scaffolds. *Mater Today Bio*. 2022;16. doi:10.1016/j.mtbio.2022.100343

760 55. Steele JAM, Moore AC, St-Pierre JP, et al. In vitro and in vivo investigation of a zonal
761 microstructured scaffold for osteochondral defect repair. *Biomaterials*. 2022;286.
762 doi:10.1016/j.biomaterials.2022.121548

763 56. Park DY, Min BH, Park SR, et al. Engineered cartilage utilizing fetal cartilage-derived progenitor
764 cells for cartilage repair. *Sci Rep*. 2020;10(1):1-13. doi:10.1038/s41598-020-62580-0

765 57. Zeng J, Huang L, Xiong H, et al. Injectable decellularized cartilage matrix hydrogel encapsulating
766 urine-derived stem cells for immunomodulatory and cartilage defect regeneration. *NPJ Regen*
767 *Med*. 2022;7(1):1-12. doi:10.1038/s41536-022-00269-w

768 58. Golchin A, Shams F, Karami F. Advancing Mesenchymal Stem Cell Therapy with CRISPR/Cas9 for
769 Clinical Trial Studies. In: *Cell Biology and Translational Medicine,*. Vol 8. ; 2019:89-100.
770 doi:10.1007/5584_2019_459

771 59. Hazrati A, Malekpour K, Soudi S, Hashemi SM. CRISPR/Cas9-engineered mesenchymal
772 stromal/stem cells and their extracellular vesicles: A new approach to overcoming cell therapy
773 limitations. *Biomedicine & Pharmacotherapy*. 2022;156:113943.
774 doi:10.1016/j.biopha.2022.113943

775 60. Chen Z, Klein T, Murray RZ, et al. Osteoimmunomodulation for the development of advanced
776 bone biomaterials. *Materials Today*. 2016;19(6):304-321. doi:10.1016/j.mattod.2015.11.004

777 61. Xie Y, Hu C, Feng Y, et al. Osteoimmunomodulatory effects of biomaterial modification strategies
778 on macrophage polarization and bone regeneration. *Regen Biomater*. 2020;7(3):233-245.
779 doi:10.1093/rb/rbaa006

780 62. Aamodt JM, Grainger DW. Extracellular matrix-based biomaterial scaffolds and the host
781 response. *Biomaterials*. 2016;86:68-82. doi:10.1016/j.biomaterials.2016.02.003

782 63. Ramakrishnaiah Siddappa, Ruud Licht, Clemens van Blitterswijk J de B. Donor variation and loss of
783 multipotency during in vitro expansion of human mesenchymal stem cells for bone tissue
784 engineering. *Journal of Orthopaedic Research*. 2007;25(8).

785 64. LaFleur MW, Nguyen TH, Coxe MA, et al. A CRISPR-Cas9 delivery system for in vivo screening of
786 genes in the immune system. *Nat Commun*. 2019;10(1):1-10. doi:10.1038/s41467-019-09656-2

787 65. Bock C, Datlinger P, Chardon F, et al. High-content CRISPR screening. *Nature Reviews Methods*
788 *Primers*. 2022;2(1). doi:10.1038/s43586-021-00093-4

789 66. Maehara H, Sotome S, Yoshii T, et al. Repair of large osteochondral defects in rabbits using
790 porous hydroxyapatite/collagen (HAp/Col) and fibroblast growth factor-2 (FGF-2). *Journal of*
791 *Orthopaedic Research*. 2010;28(5):677-686. doi:10.1002/jor.21032

792

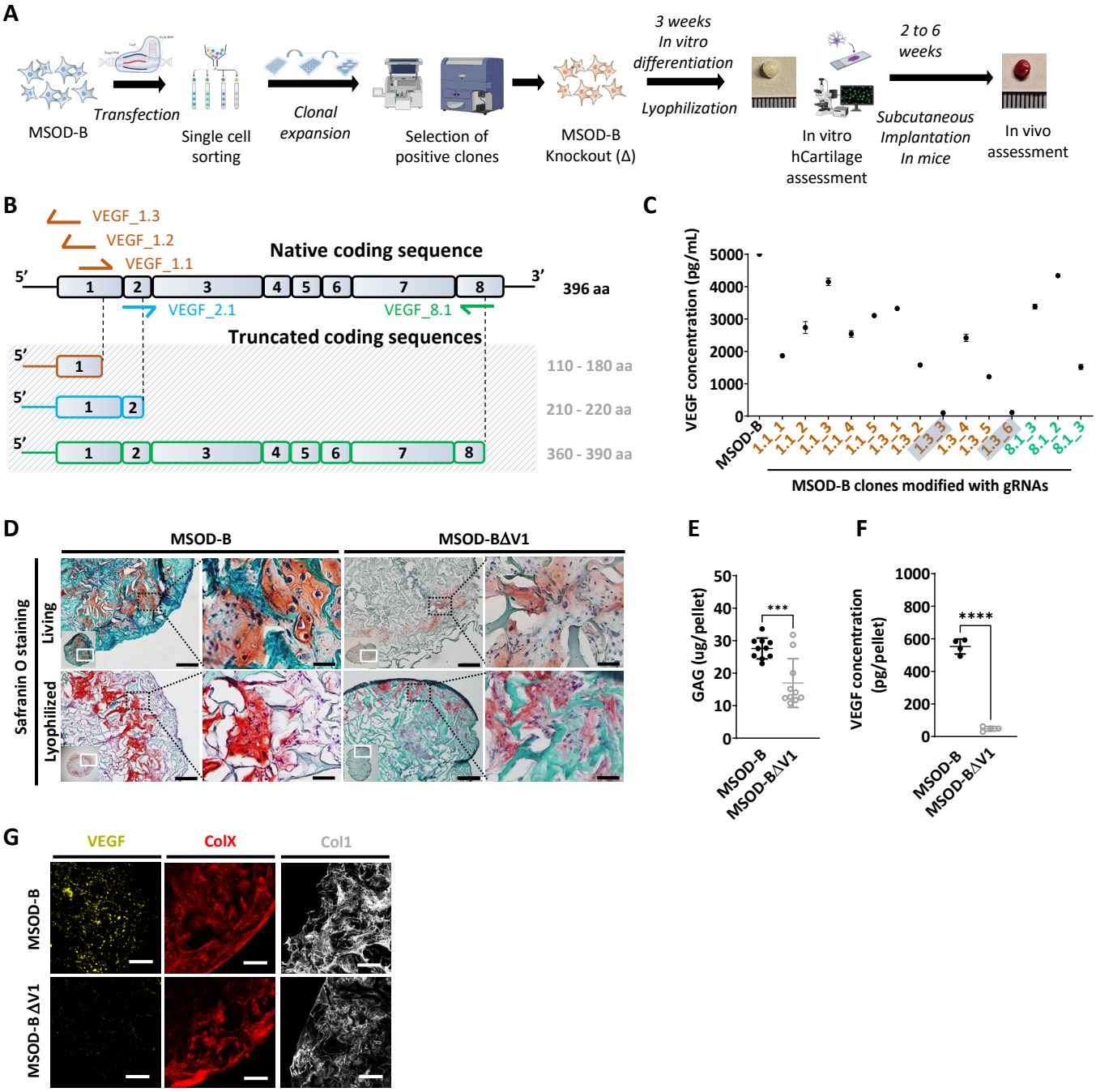

Figure 1. CRISPR/Cas9 editing of mesenchymal cell lines lead to efficient VEGF knockout in cartilage tissues. A) Experimental scheme depicting the generation of CRISPR/Cas9-edited MSOD-B lines, and the subsequent in vitro and in vivo tissue formation assessment. B) Overview of the native human VEGF coding sequence composed of eight exons. Designed gRNAs and their targeted binding sites are illustrated, as well as the corresponding expected impact on the coding sequence. gRNAs targeting exon 1 (orange) disrupt translation initiation and inhibit protein expression, gRNA targeting exon 2 (blue) disrupts VEGF receptor binding, and gRNA targeting exon 8 (green) alters the C-Terminal sequence and repress activation of protein. C) ELISA-based quantitative analysis of VEGF protein content in cell culture supernatant from expanded single cell colonies. From all clones, only two had no detectable level of VEGF (1.3_3 and 1.3_6). These clones were subsequently defined as MSOD-BΔV1 and MSOD-BΔV2. D) Histological assessment of living and lyophilized in vitro differentiated constructs using Safranin O staining (Scale bars = 100 µm and 20 µm for magnified areas). Both the MSOD-B and MSOD-BΔV1 displayed glycosaminoglycans (GAG) (orange to reddish in Safranin O), indicating successful cartilage formation (Scale bars = 200 µm). Left bottom inserts show the whole tissue section. E) Quantitative assessment of the total GAG content in MSOD-B and MSOD-BΔV1 in vitro differentiated constructs, post-lyophilization. Unpaired t-test, n = 10 biological replicates, ***$p < 0.001$. F) ELISA-based quantitative assessment of VEGF protein in in vitro differentiated constructs, post-lyophilization. Unpaired t-test, n = 3-4 biological replicates, ****$p < 0.0001$. G) Immunofluorescence images of MSOD-B and MSOD-BΔV1 tissues, post-lyophilization. Displayed images consist of 3D-stacks from 80-100 µm thick sections, stained for VEGF (yellow), Collagen Type X (COLX, red) and Collagen Type I (COL1, grey). A clear reduction in the VEGF signal could be observed in the MSOD-BΔV1 tissues, indicating a successful VEGF knockdown (Scale bars = 80 µm).

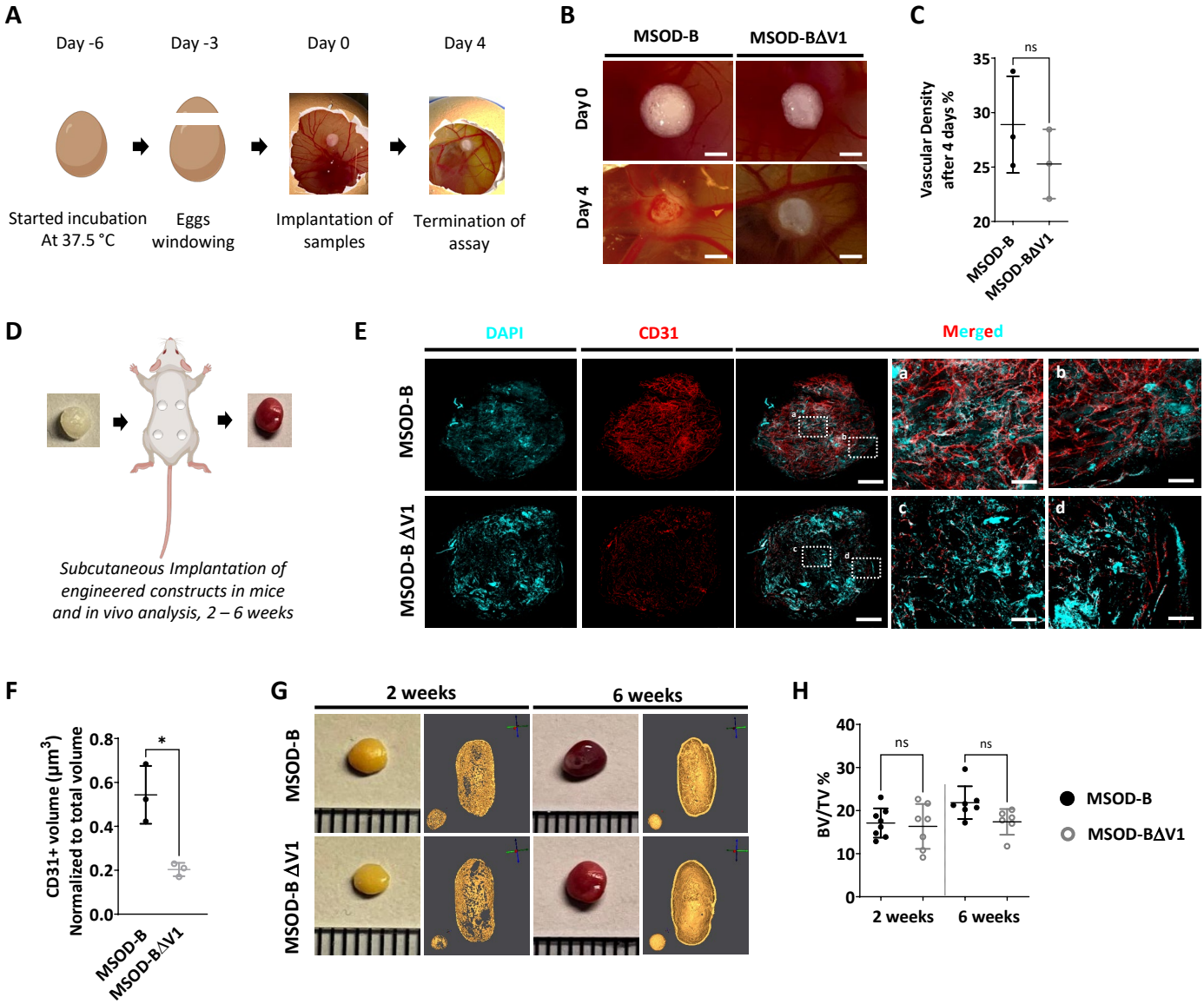
A
Day -6
Day -3
Day 0
Day 4
Started incubation At 37.5 °C
Eggs windowing
Implantation of samples
Termination of assay
B
MSOD-B
MSOD-BΔV1
Day 0
Day 4
C
ns
Vascular Density after 4 days %
35
30
25
20
MSOD-B
MSOD-BΔV1
D
Subcutaneous Implantation of engineered constructs in mice and in vivo analysis, 2 – 6 weeks
E
DAPI
CD31
Merged
MSOD-B
MSOD-B ΔV1
a
b
c
d
F
*
CD31+ volume (µm³) Normalized to total volume
0.8
0.6
0.4
0.2
0.0
MSOD-B
MSOD-BΔV1
G
2 weeks
6 weeks
MSOD-B
MSOD-B ΔV1
H
ns
ns
BV/TV %
40
30
20
10
0
2 weeks
6 weeks
MSOD-B
MSOD-BΔV1
I
2 weeks
6 weeks
Safranin O
Masson's Trichrome
Safranin O
Masson's Trichrome
MSOD-B
MSOD-BΔV1
CB
BM
TB

Figure 2. VEGF knockout cartilage tissues retain bone remodeling capacity despite reduced early-stage vascularization

A) Experimental scheme of the Chorioallantoic Membrane (CAM) assay, for ex vivo evaluation of angiogenic potential. B) Macroscopic comparison of in vitro MSOD-B and MSOD-BΔV1 constructs at day 0 (day of implantation) and day 4 (4 days post-implantation), illustrating robust de novo vessel formation perfusing the tissues (Scale bars at 1 mm). C) Quantitative Analysis of Vascular Density in MSOD-B and MSOD-BΔV1. Vascular densities were quantified from macroscopic images obtained on day 4 using ImageJ. Unpaired t-test, n = 3-4 biological replicates, n.s. = not significant. D) overview of the subcutaneous implantation procedure in mice and subsequent in vivo evaluation of vascularization from 2 to 6 weeks post-implantation. E) Immunofluorescence images of MSOD-B and MSOD-BΔV1 tissues two weeks post-in vivo implantation. Displayed images consist of 3D-stacks from 80-100 µm thick sections, vessels stained with mouse CD31 (red) and nuclei with DAPI (cyan) (Scale bars at 500 µm except for magnified white inserts at 80 µm). Box "a" and "c" display the periphery whereas Box "b" and "d" show the central region of MSOD-B and MSOD-BΔV1 constructs respectively. A reduction in tissue vascularization is observed in MSOD-BΔV1 samples. F) Quantitative analysis of the CD31 signal using an isosurface-based strategy (IMARIS software). Unpaired t-test, n = 3-4 biological replicates, *$p < 0.05$. G) Representative macroscopic and microtomography images of in vivo constructs retrieved at two and six weeks post-implantation. H) Microtomography-based quantification of the sample's bone/ mineralized volume over their total volume (ratio). No significant differences between MSOD-B and MSOD-BΔV1 could be observed. (BV: Bone Volume, TV: Total Volume). Ordinary One-way ANOVA, n=8 biological replicates, n.s.=not significant I) Histological analysis of in vivo tissues using Safranin O and Masson's trichrome stains, at two (2W) and six weeks (6W) post-implantation. Both sample types underwent full remodeling into a bone organ after 6 weeks, with presence of bone structures and a bone marrow compartment (Scale bars = 200 µm). CB – cortical bone; BM – bone marrow. TB – trabecular bone.

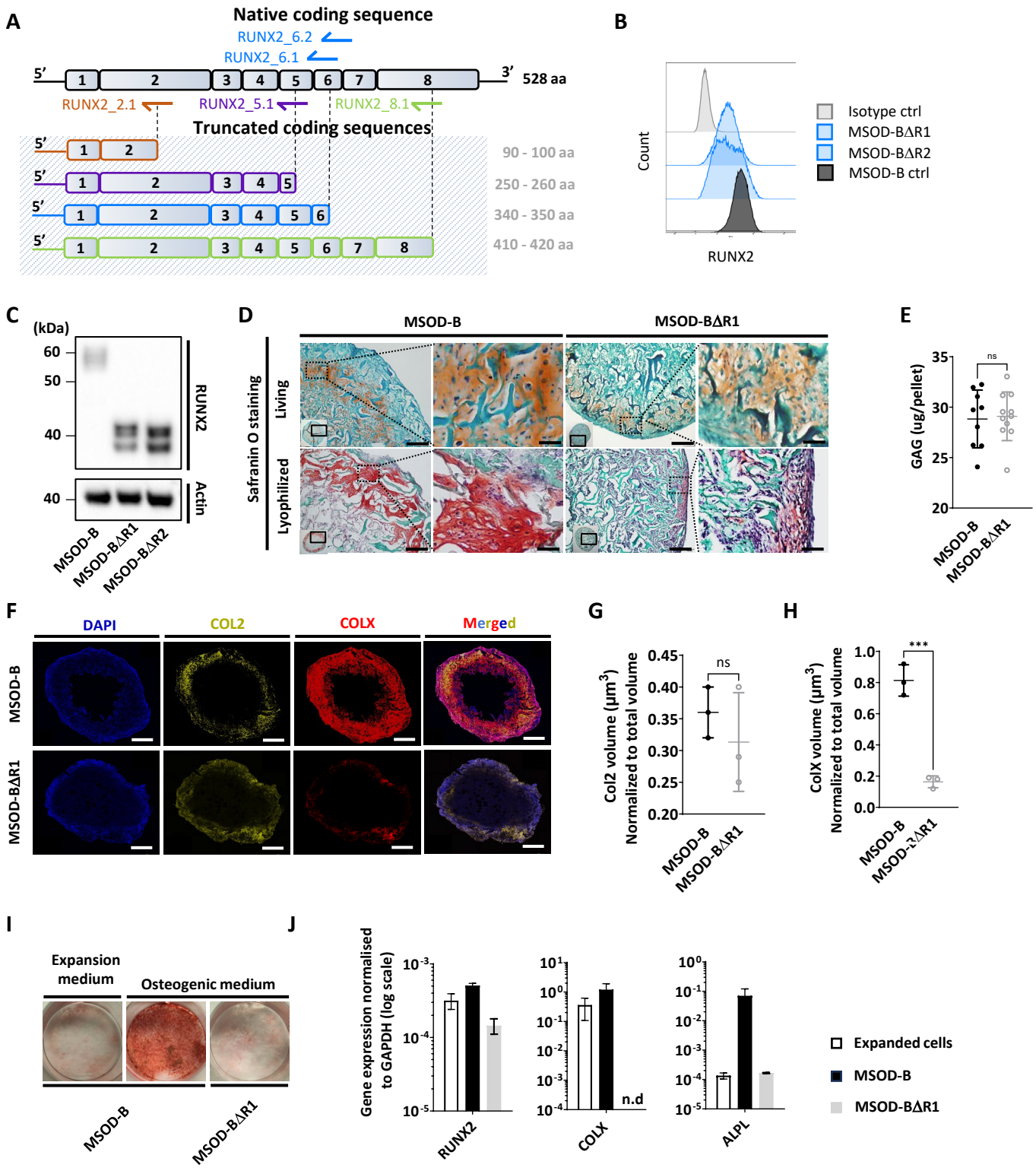
A
Native coding sequence
RUNX2_6.2
RUNX2_6.1
5'
1
2
3
4
5
6
7
8
3'
528 aa
RUNX2_2.1
RUNX2_5.1
RUNX2_8.1
Truncated coding sequences
90 - 100 aa
250 - 260 aa
340 - 350 aa
410 - 420 aa
B
Count
RUNX2
Isotype ctrl
MSOD-BΔR1
MSOD-BΔR2
MSOD-B ctrl
C
(kDa)
60
50
40
40
RUNX2
Actin
MSOD-B
MSOD-BΔR1
MSOD-BΔR2
D
MSOD-B
MSOD-BΔR1
Safranin O staining
Living
Lyophilized
E
GAG (ug/pellet)
35
30
25
20
ns
MSOD-B
MSOD-BΔR1
F
DAPI
COL2
COLX
Merged
MSOD-B
MSOD-BΔR1
G
Col2 volume (µm³)
Normalized to total volume
0.45
0.40
0.35
0.30
0.25
0.20
ns
MSOD-B
MSOD-BΔR1
H
ColX volume (µm³)
Normalized to total volume
1.0
0.8
0.6
0.4
0.2
0.0
***
MSOD-B
MSOD-BΔR1
I
Expansion medium
Osteogenic medium
MSOD-B
MSOD-BΔR1
J
Gene expression normalised to GAPDH (log scale)
10⁻³
10⁻⁴
10⁻⁵
10¹
10⁰
10⁻¹
10⁻²
10⁻³
10⁻⁴
10⁰
10⁻¹
10⁻²
10⁻³
10⁻⁴
10⁻⁵
n.d
RUNX2
COLX
ALPL
Expanded cells
MSOD-B
MSOD-BΔR1

Figure 3. RUNX2 knockout does not prevent chondrogenic differentiation but impairs hypertrophy A) Overview of the human RUNX2 coding sequence comprising 8 exons. gRNAs and their corresponding expected protein structure. The gRNA targeting exon 2 (orange) disrupts the DNA binding domain, gRNA targeting exon 5 (violet) disrupts nuclear translocation, gRNAs targeting exon 6 (blue) disrupt the transcriptional activation domain and gRNAs targeting exon 8 (green) disrupt the nuclear matrix targeting signal and repress the protein function. B) Intracellular flow cytometry for RUNX2 detection in MSOD-B and RUNX2-edited clones. A clear protein reduction could be observed in the 6.1_1 and 6.1_23 clones. C) Western blot analysis of RUNX2 in cultured MSOD-B and RUNX2-edited cells. The genetic editing of RUNX2 is confirmed by the detection of the truncated proteins. Actin is used as a control to normalize the protein content. D) Histological analysis of living and lyophilized in vitro differentiated constructs using Safranin O staining (Scale bars = 100 µm and 20 µm for magnified areas), indicating the presence of cartilage matrices. E) Quantitative assessment of the total GAG content in corresponding in vitro generated lyophilized tissues. Unpaired t-test, n=10-11 biological replicates **$p < 0.01$. F) Immunofluorescence images of MSOD-B and MSOD-B∆R1 lyophilized tissues. Displayed images consist of 3D-stacks from 80-100 µm thick sections, stained for DAPI (blue), Collagen Type II (COL2, yellow) and Collagen Type X (COLX, red). A clear reduction in the COLX signal could be observed in the MSOD-B∆R1 tissues, indicating impaired hypertrophy. (Scale bars = 500 µm) G) Isosurface-based quantification of the COL2 immunofluorescent signal using the IMARIS software. No significant difference between groups confirm the retention of cartilage formation in RUNX2-edited constructs. Unpaired t-test, n=3 biological replicates, n.s.=not significant. H) Isosurface-based quantification of the COLX immunofluorescent signal using the IMARIS software, confirming the disruption of hypertrophy in the MSOD-B∆R1 constructs. Unpaired t-test, n=3, ***$p < 0.001$. I) Alizarin Red staining evidencing a lack of mineralization in the MSOD-B∆R1 culture compared to the MSOD-B. J) Quantitative PCR analysis displaying the relative expression levels of osteogenesis-related genes: RUNX2, COL1, and ALPL. The expression is normalized to GAPDH as housekeeping gene. n.d= not detected.

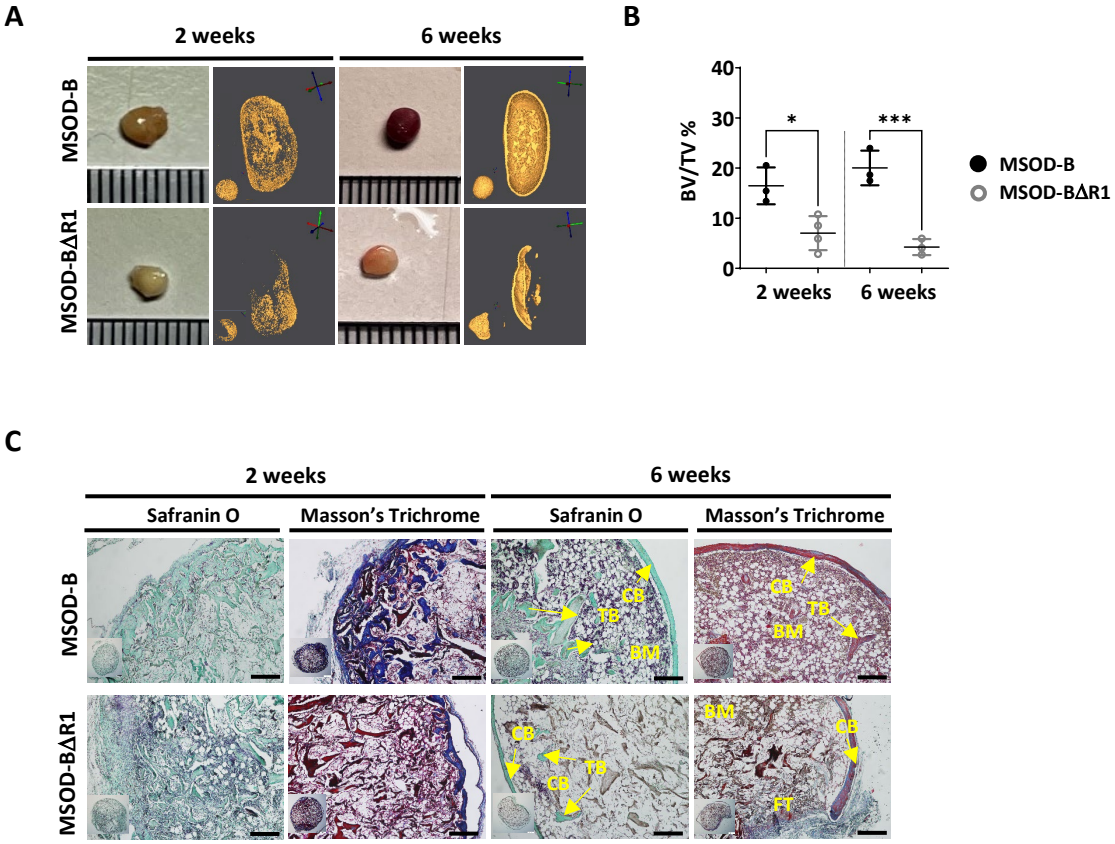

Figure 4. RUNX2 knockout in cartilage tissues disrupts effective ectopic bone formation A) Representative macroscopic and microtomography images of in vivo constructs retrieved at two and six weeks post-implantation. B) Microtomography-based quantification of the sample's bone/mineralized volume over their total volume (ratio). (BV: Bone Volume, TV: Total Volume). A marked difference is observed as early as two weeks, with a clear lower mineral content in MSOD-BΔR1 samples. Ordinary one way ANOVA, n=3 biological replicates, *$p < 0.05$, ***$p < 0.001$. C) Histological analysis of in vivo constructs using Safranin O and Masson's trichrome stains. After two weeks (2W), a higher bone formation is already evident in the MSOD-B control group. The MSOD-BΔR1 samples explanted after 6 weeks (6W) displayed presence of cortical and trabecular bone, but also large amount of fibrous tissue indicating an incomplete remodeling. (Scale bars = 200 µm).

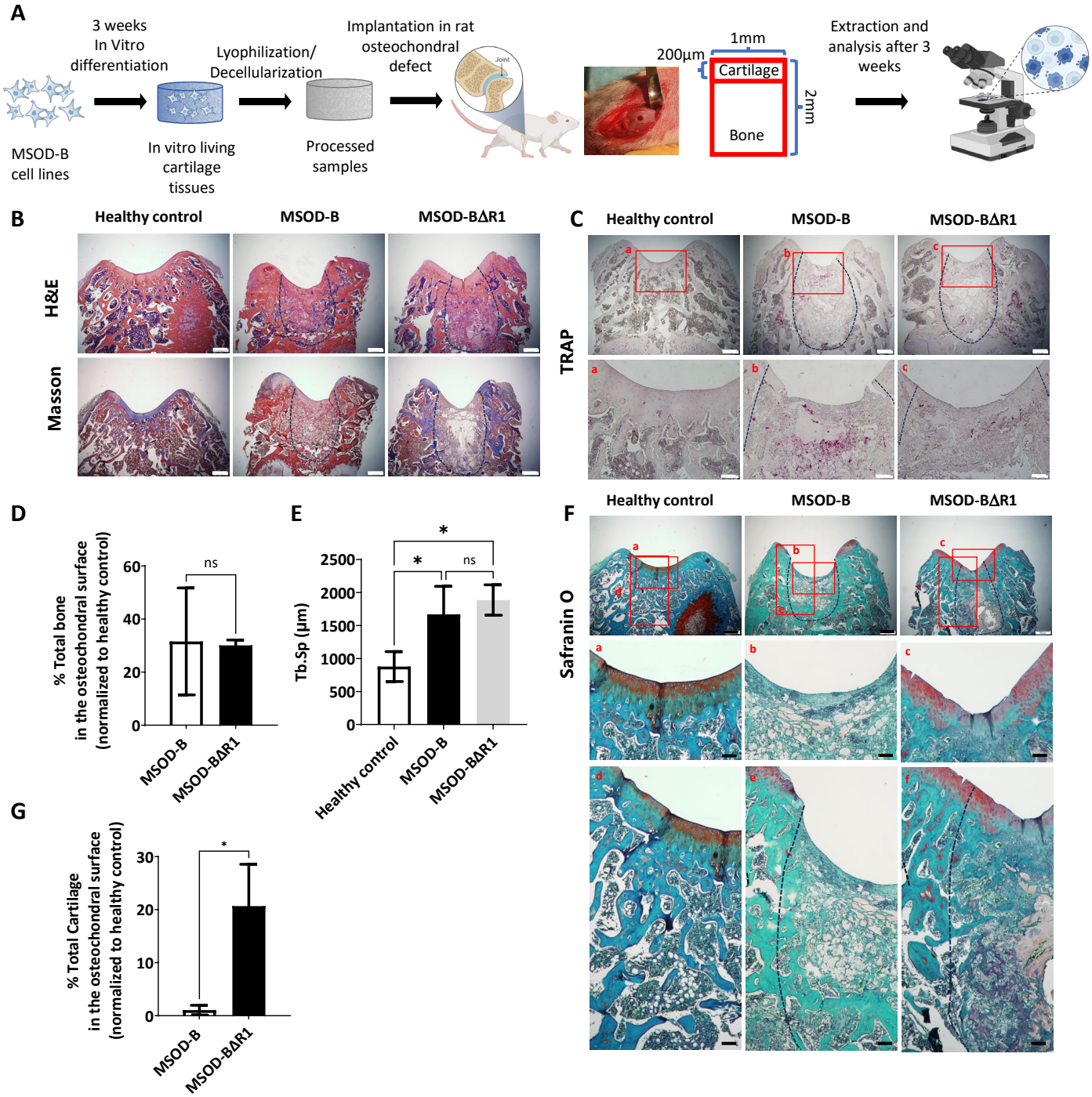

Figure 5. RUNX2 knockout in cartilage tissues leads to better cartilage regeneration and maintenance in osteochondral defect in rats A) Experimental scheme for the regenerative potential assessment of MSOD-B & MSOD-BΔR1 cartilage tissues in a rat osteochondral defect. B) Histological analysis of the osteochondral defects for each group using H&E and Masson's trichrome stains, at three weeks post-implantation. The dash-line marks the defect area. (Scale bars = 500 µm) C) Histological analysis the osteochondral defects using TRAP staining reporting osteoclastic activity, at three weeks post-implantation. The dash-line marks the defect area. (Scale bars = 500 µm and 100 µm for magnified areas) D) Microtomography-based quantification of the sample's total bone/mineralized volume normalized to the healthy control in percentage. Unpaired t-test, n=3 biological replicates, n.s.=not significant. E) Image J based quantification of Trabecular separation (Tb.Sp). One way ANOVA test, n=3 biological replicates, *$p < 0.05$ F) Histological analysis of the osteochondral defects using Safranin O staining. After three weeks, a higher regeneration of the surface cartilage is evident in the MSOD-BΔR1 group (a,b,c) (Scale bars = 500 µm and 100 µm for magnified areas). The magnified regions of the subchondral area (d,e,f) show higher cartilage remnants and integration in the MSOD-BΔR1 group. G) Quantitative analysis of cartilage regeneration in the osteochondral surface as compare to the healthy control (100%). Unpaired t-test, n=3 biological replicates, *$p < 0.05$.

Table 1: Scoring rate for individual categories

Semi-quantitative analysis utilizing a modified histological grading system, including parameters such as cellular morphology, matrix staining, surface regularity, thickness of cartilage, subchondral bone formation and integration of adjacent cartilage , resulting in a comprehensive assessment of tissue regeneration and integration

	Scoring Rate (%) (SD)					
	Cell Morphology	Matrix Staining	Surface Regularity	Thickness of Cartilage	Regenerated Subchondral Bone	Integration with Adjacent Cartilage
Healthy	100 (0)	100 (0)	100 (0)	100 (0)	100 (0)	100 (0)
MSOD-B	33,33 (28,86)	16,66 (14,43)	50 (0)	8,33 (14,33)	16,66 (14,33)	33,33 (14,33)
MSOD-B ΔR1	66,66 (14,33)	50 (0)	41,66 (14,33)	33,33 (28,86)	25 (25)	50 (0)

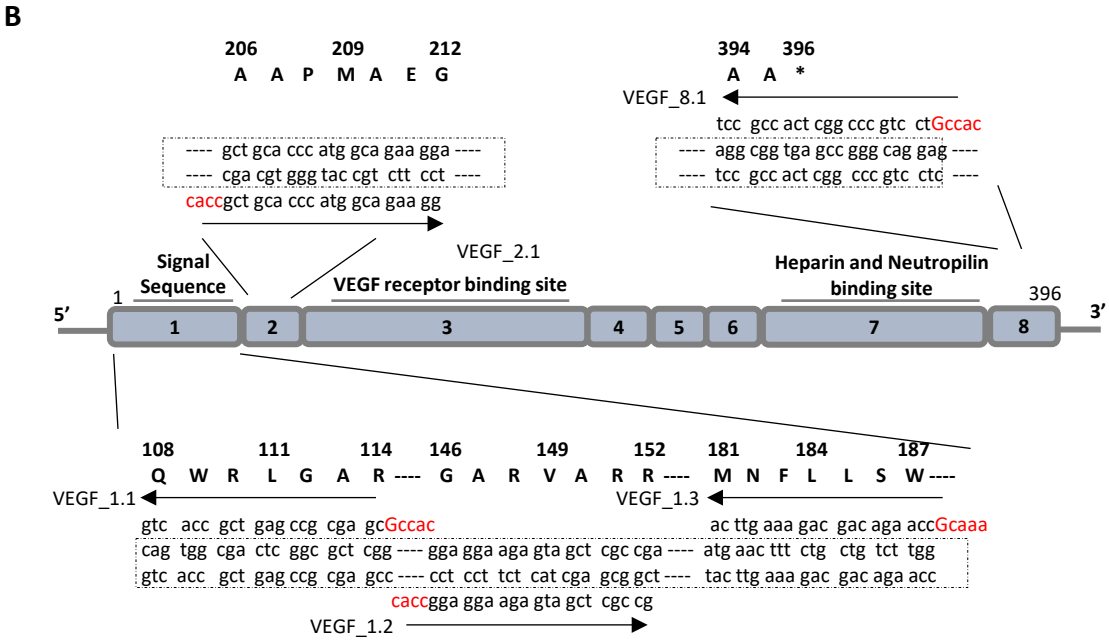

Supplementary figure 1. **CRISPR/Cas9 editing of mesenchymal cell lines lead to efficient VEGF knockout in cartilage tissues.** A) Implemented genetic elements of the Mesenchymal Sword Of Damocles BMP-2 (MSOD-B) cells consisting of the human telomerase reverse transcriptase (hTERT), an inducible caspase 9 (iCaspase) death system and the bone morphogenetic protein type-2. All systems are constitutively expressed and further described in Pigeot et al. Advanced Materials 2021. B) Overview of the human VEGF exon structure, nucleotide sequences of targeting gRNAs and their corresponding amino acid sequences.

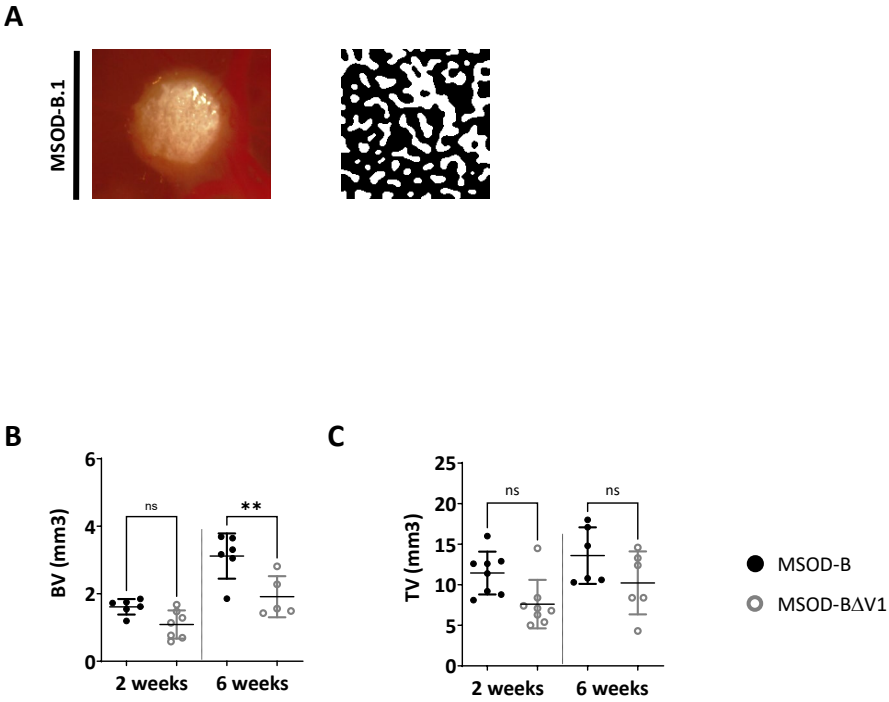

Supplementary figure 2. VEGF knockout cartilage tissues retain bone remodeling capacity despite reduced early-stage vascularization. A) Sequential processing of a vascular tissue section using Q-VAT, depicting the original image, binary mask creation, and vessel segmentation for quantitative vascular density analysis. B) Microtomography analysis (Bone/mineralized volume) showed significant differences between in vivo constructs at both two weeks and six weeks time points (One way ANOVA, n=3, **$p < 0.01$, n.s.= not significant). C) Microtomography analysis (total volume) did not show significant difference between in vivo constructs at either two weeks or six weeks time points (One way ANOVA, n=3, n.s.= not significant) (BV: Bone Volume, TV: Total Volume).

A

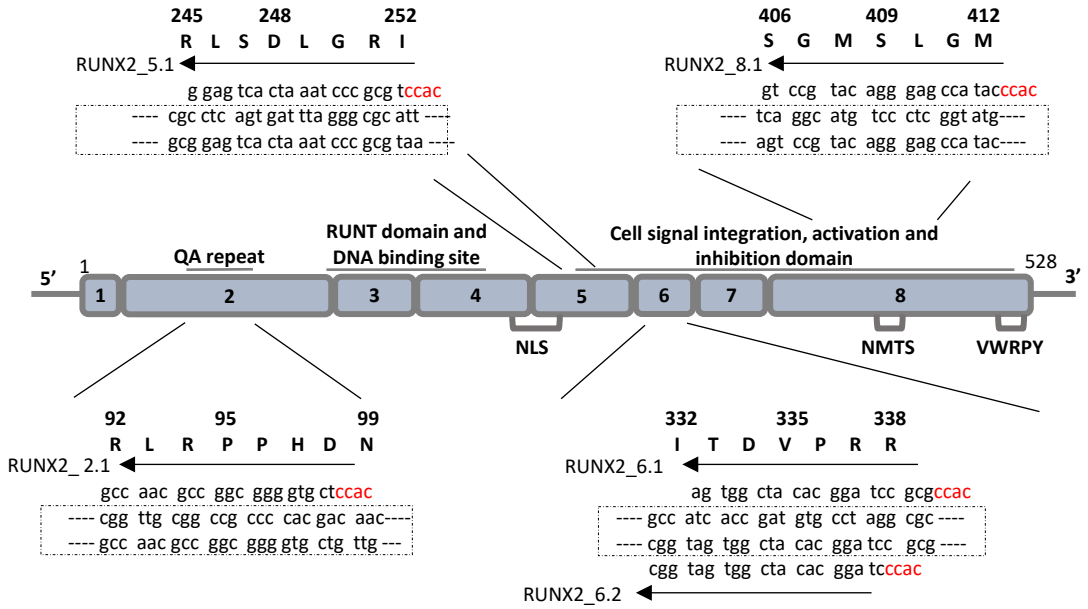
245 248 252
R L S D L G R I
RUNX2_5.1
g gag tca cta aat ccc gcg tccac
---- cgc ctc agt gat tta ggg cgc att ----
---- gcg gag tca cta aat ccc gcg taa ----
406 409 412
S G M S L G M
RUNX2_8.1
gt ccg tac agg gag cca taccccac
---- tca ggc atg tcc ctc ggt atg----
---- agt ccg tac agg gag cca tac----
RUNT domain and DNA binding site
Cell signal integration, activation and inhibition domain
QA repeat
5'
1
528
3'
1 2 3 4 5 6 7 8
NLS
NMTS
VWRPY
92 95 99
R L R P P H D N
RUNX2_ 2.1
gcc aac gcc ggc ggg gtg ctccac
---- cgg ttg cgg ccg ccc cac gac aac----
---- gcc aac gcc ggc ggg gtg ctg ttg ---
332 335 338
I T D V P R R
RUNX2_6.1
ag tgg cta cac gga tcc gcgccac
---- gcc atc acc gat gtg cct agg cgc ----
---- cgg tag tgg cta cac gga tcc gcg ----
cgg tag tgg cta cac gga tcccac
RUNX2_6.2

B

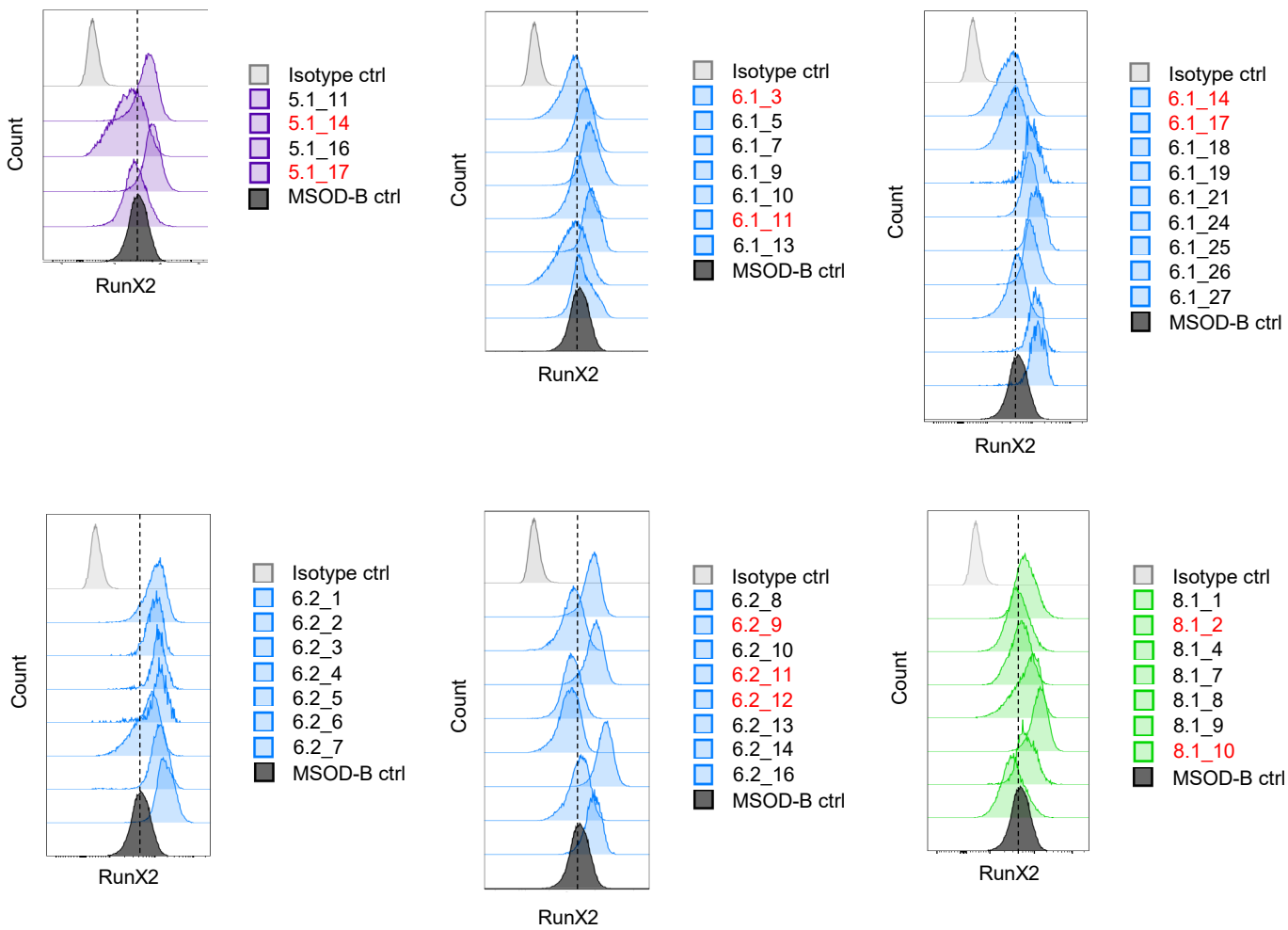
Count
RunX2
Isotype ctrl
5.1_11
5.1_14
5.1_16
5.1_17
MSOD-B ctrl
Isotype ctrl
6.1_3
6.1_5
6.1_7
6.1_9
6.1_10
6.1_11
6.1_13
MSOD-B ctrl
Isotype ctrl
6.1_14
6.1_17
6.1_18
6.1_19
6.1_21
6.1_24
6.1_25
6.1_26
6.1_27
MSOD-B ctrl
Isotype ctrl
6.2_1
6.2_2
6.2_3
6.2_4
6.2_5
6.2_6
6.2_7
MSOD-B ctrl
Isotype ctrl
6.2_8
6.2_9
6.2_10
6.2_11
6.2_12
6.2_13
6.2_14
6.2_16
MSOD-B ctrl
Isotype ctrl
8.1_1
8.1_2
8.1_4
8.1_7
8.1_8
8.1_9
8.1_10
MSOD-B ctrl

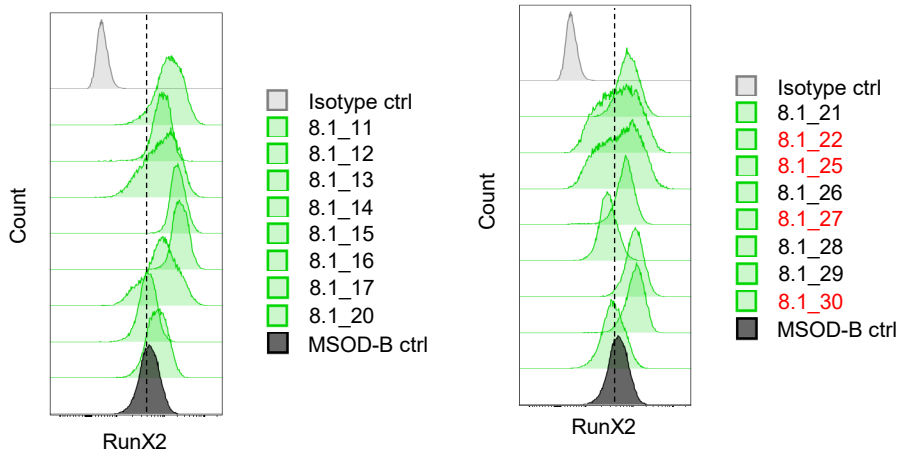
Count
RunX2
Isotype ctrl
8.1_11
8.1_12
8.1_13
8.1_14
8.1_15
8.1_16
8.1_17
8.1_20
MSOD-B ctrl
Count
RunX2
Isotype ctrl
8.1_21
8.1_22
8.1_25
8.1_26
8.1_27
8.1_28
8.1_29
8.1_30
MSOD-B ctrl

C

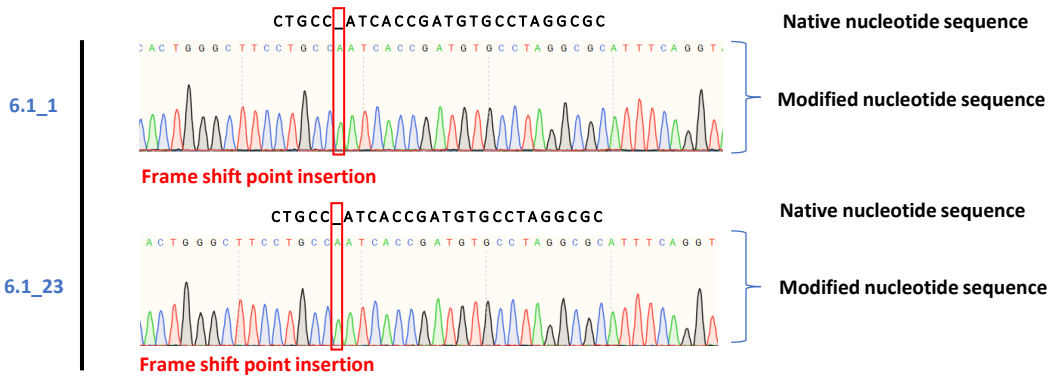
CTGCC_ATCACCGATGTGCCTAGGCGC
Native nucleotide sequence
6.1_1
Modified nucleotide sequence
Frame shift point insertion
CTGCC_ATCACCGATGTGCCTAGGCGC
Native nucleotide sequence
6.1_23
Modified nucleotide sequence
Frame shift point insertion

D

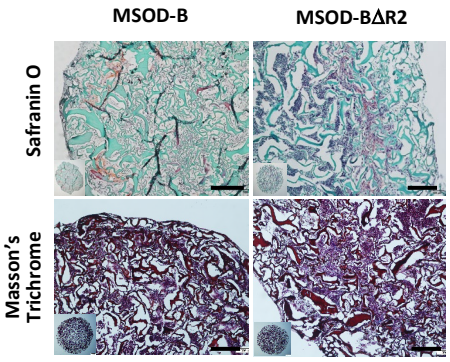
MSOD-B
MSOD-BΔR2
Safranin O
Masson's Trichrome

E

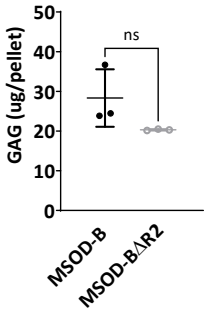
GAG (ug/pellet)
50
40
30
20
10
0
ns
MSOD-B
MSOD-BΔR2

F

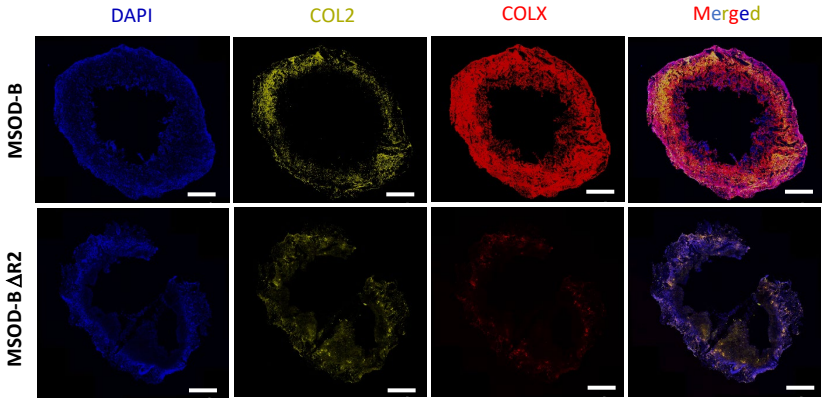
DAPI
COL2
COLX
Merged
MSOD-B
MSOD-B ΔR2

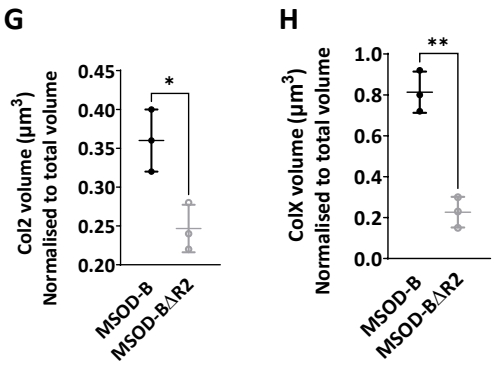

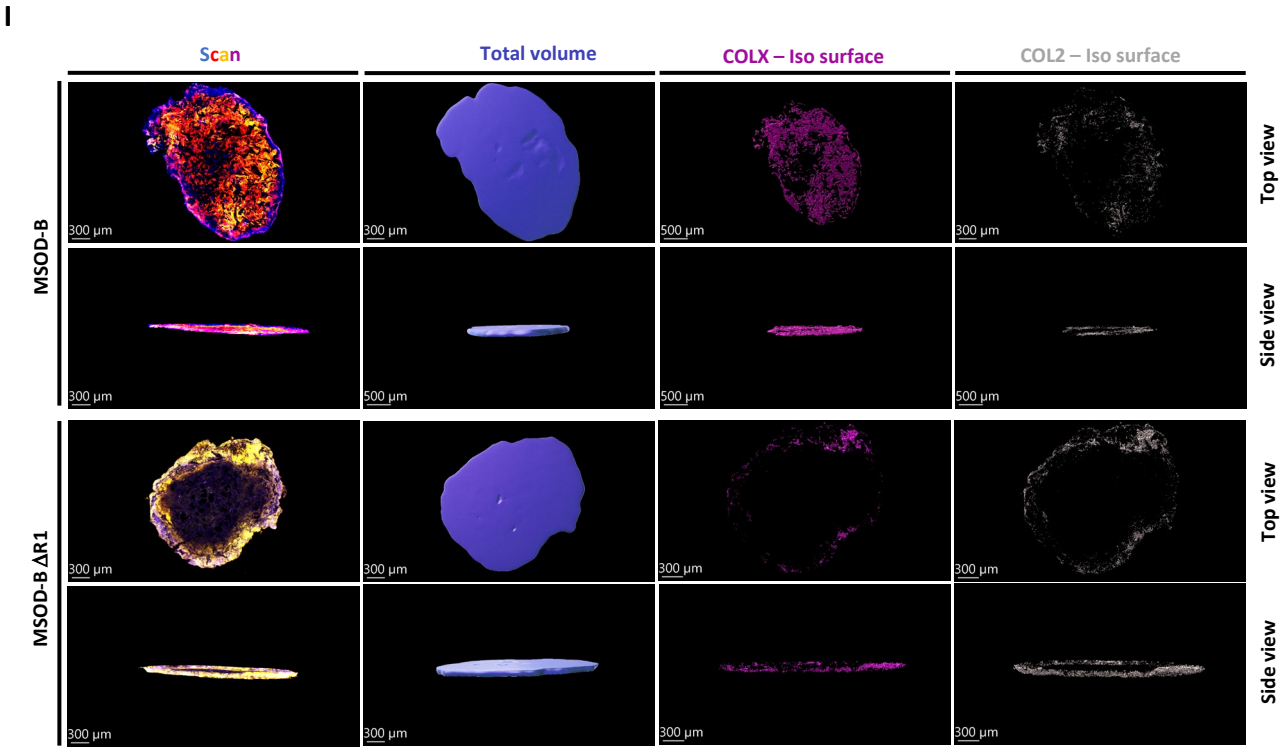

Supplementary figure 3. RUNX2 knockout does not prevent chondrogenic differentiation but impairs hypertrophy A) Overview of human RUNX2 exon structure, nucleotide sequences of targeting gRNAs and its corresponding amino acid sequence. B) Intracellular flow cytometry for RUNX2 detection in MSOD-B and RUNX2-edited clones. Clones whose peaks fell left of the dotted line were selected for sequencing. C) Sanger sequencing results of DNA extracted from MSOD-BΔR samples and the modifications compared to MSOD-B DNA sequence. D) Histological analysis of in vitro constructs from using Safranin O and Masson trichrome staining displayed the presence of glycosaminoglycans (GAG) and collagen content respectively, indicating the presence of cartilage formation in MSOD-BΔR2 (Scale bars = 200 µm). E) Quantitative assessment of the total GAG content confirms the presence of cartilage formation in both constructs thus confirming RUNX2 knockout in hMSCs (MSOD-BΔR2) retain cartilage formation. (unpaired t-test, n=3, n.s. = not significant). F) Reduction of RUNX2 expression in cartilage tissues lead to reduced hypertrophy. Representative immunofluorescence staining images of COL2, COLX and DAPI tissue section of in vitro cartilage constructs shows reduction of COLX expression in knockout construct (MSOD-BΔR2) indicating reduction of hypertrophy. (Scale bars = 500 µm). G) Quantitative analysis of the immunofluorescent staining sections using IMARIS software displayed significant difference in the expression of COL2, demonstrating reduction of cartilage formation in knockout constructs (MSOD-BΔR2) (unpaired t-test, n=3, *$p < 0.05$). H) Quantitative analysis of the immunofluorescent staining sections using IMARIS software displayed a significant reduction in expression of COLX, confirming the disruption of hypertrophy in knockout constructs (unpaired t-test, n=3, **$p < 0.01$). I) Representative isosurface images of immunofluorescent staining sections constructed using IMARIS software.

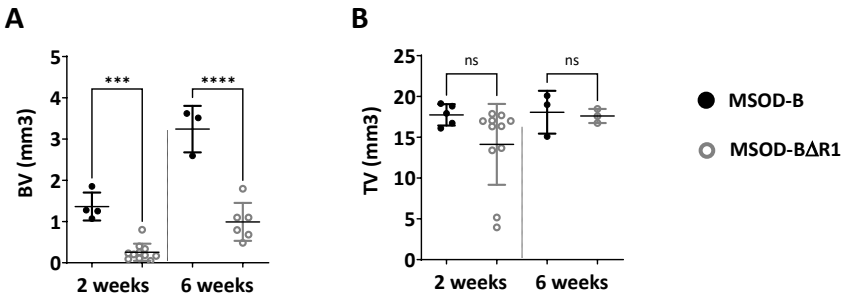

Supplementary figure 4. **RUNX2 knockout in cartilage tissues disrupts effective bone formation.** A) Microtomography analysis (Bone/mineralized volume) showed very high significant difference between in vivo constructs at both two weeks and six weeks time points (One was ANOVA, n=3, ***p < 0.001, ****p < 0.0001). B) Microtomography analysis (total volume) showed significant difference between in vivo constructs at two weeks time point but no significant difference at six weeks time point (One was ANOVA, n=3, n.s. = not significant) (BV: Bone Volume, TV: Total Volume).

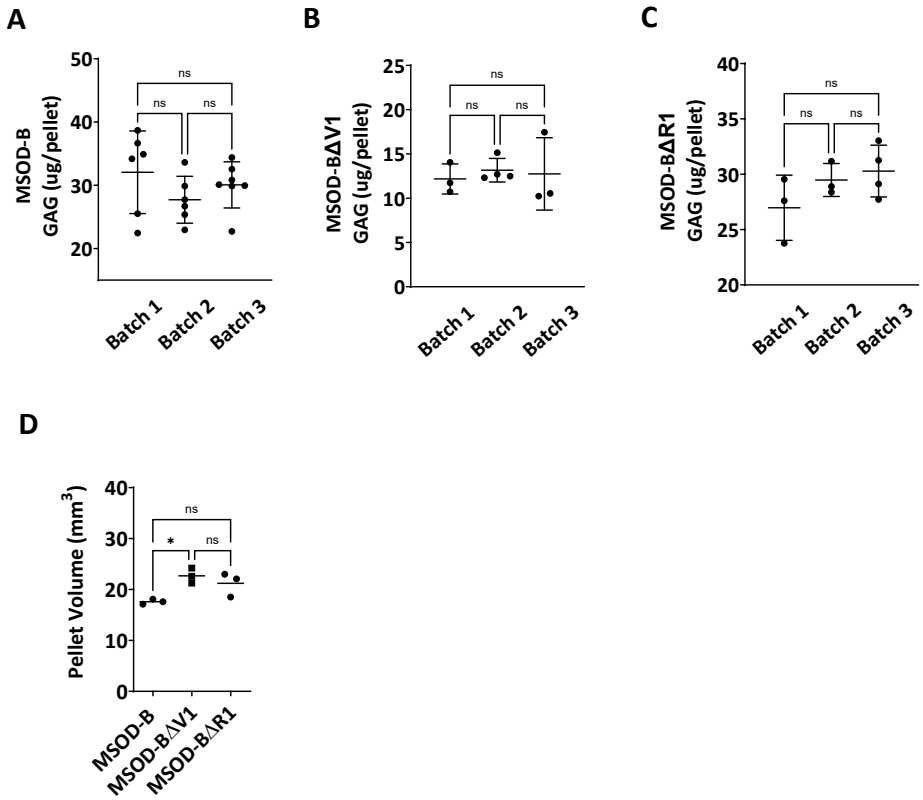

Supplementary figure 5. **Characterization of engineered cartilage tissues post-lyophilization.** A) Quantitative assessment of the total GAG content in MSOD-B in vitro differentiated constructs across three different batch productions. One way ANOVA test, n=6-7 biological replicates, n.s. = not significant. B) Quantitative assessment of the total GAG content in MSOD-BΔV1 in vitro differentiated constructs across three different batch productions. One way ANOVA test, n=3-4 biological replicates, n.s.=not significant. C) Quantitative assessment of the total GAG content in MSOD-BΔR1 in vitro differentiated constructs across three different batch productions. One way ANOVA test, n=3 biological replicates, ***$p < 0.001$, ****$p < 0.0001$, n.s =not significant. D) Quantitative assessment of cartilage tissue volume in MSOD-B, MSOD-BΔV1 and MSOD-BΔR1 tissues. One way ANOVA test, n=3 biological replicates, *$p < 0.05$, n.s.=not significant.

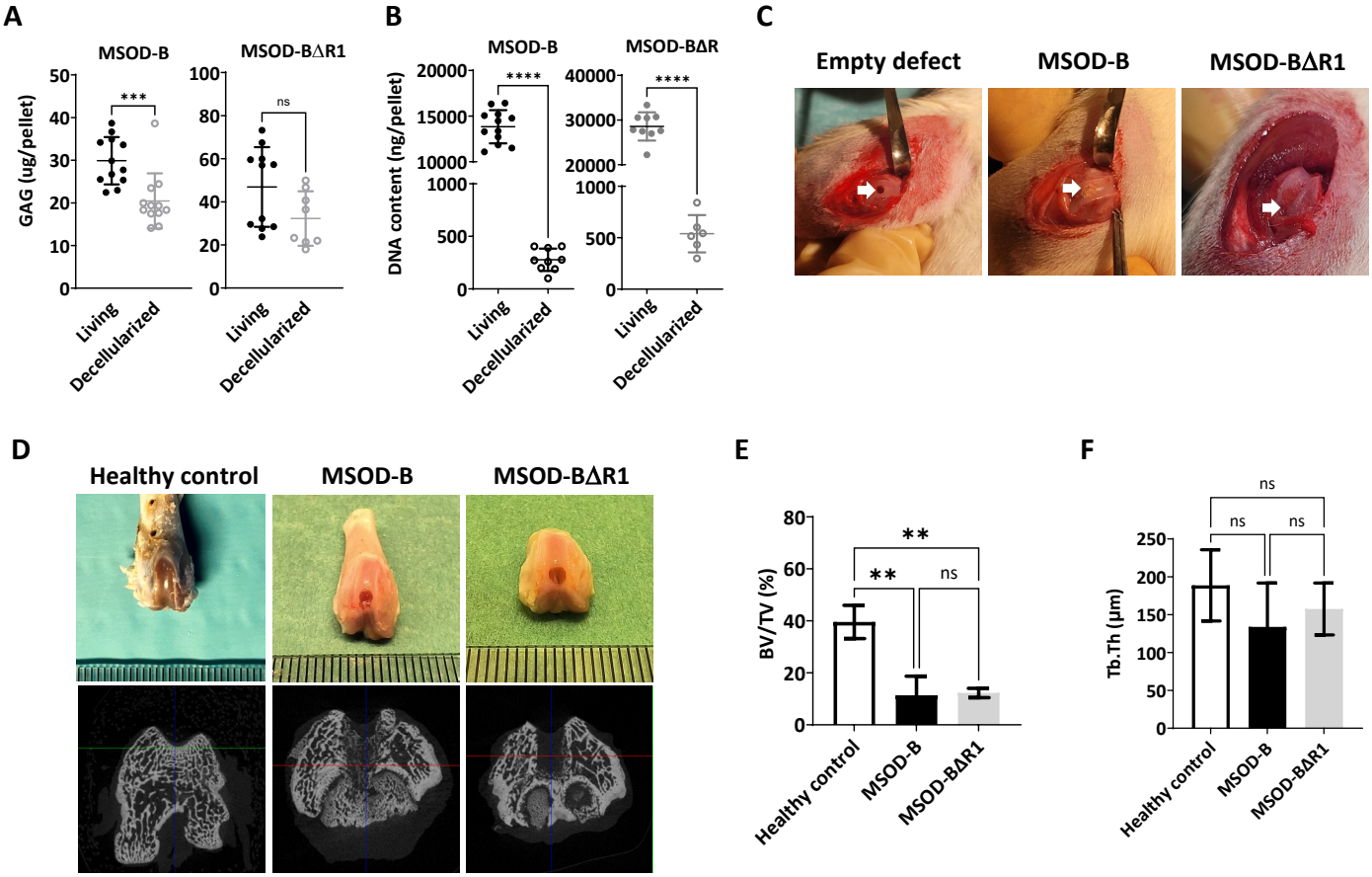

Supplementary figure 6. RUNX2 knockout in cartilage tissues exhibit better cartilage regeneration and maintenance in osteochondral defect in rats A) Quantitative assessment of the total GAG content in MSOD-B and MSOD-BΔR1 in vitro differentiated constructs before (living) and after (Decellularized) the decellularization process. unpaired t-test, n=12 biological replicates , ***p < 0.001, n.s. = not significant B) DNA quantification of in vitro engineered cartilage grafts before (living) and after (Decellularized) the decellularization process. unpaired t-test, n=12 biological replicates, ****p < 0.0001. C) Macroscopic images osteochondral defect model in rats depicting in of empty defect, defect filled with MSOD-B and defect filled with MSOD-BΔR1 respectively . D) Macroscopic images of extracted rat knees depicting healthy control without any defect, defect filled with MSOD-B and defect filled with MSOD-BΔR1 respectively and microtomography images of same respective constructs. E). No significant difference in BV/TV is observed between MSOD-B & MSOD-BΔR1 samples despite significantly reduced BV/TV ratio in both samples compared to healthy control. One way ANOVA test, n=3 biological replicates, **p < 0.01. F) Image J based quantification of Trabecular thickness (tb.Th) . One way ANOVA test, n=3 biological replicates, n.s = not significant.

Supplementary table 1: Histological grading system The histological graded system is modified and adapted from previously established model as mentioned in materials and methods section. This modified scale incorporates six distinct parameters to comprehensively evaluate the quality of tissue repair

Category	Point
Cell morphology	
Hyaline cartilage	4
Mostly hyaline cartilage or fibrocartilage	3
Mostly fibrocartilage	2
Mostly non-cartilage	1
Non-cartilage	0
Matrix-staining (metachromasia)	
Normal	3
Slightly reduced	2
Markedly reduced	1
No metachromatic staining	0
Surface regularity[a]	
Smooth	3
Moderate	2
Irregular	1
Severely irregular	0
Thickness of cartilage (%)[b]	
121–150	1
81–120	2
51–80	1
0–50	0
Regenerated subchondral bone	
Good	2
Moderate	1
Poor	0
Integration with adjacent cartilage	
Both edges integrated	2
One edge integrated	1
Neither edge integrated	0
Total maximum	16

- [a] Total smooth area of the reparative cartilage compared with the entire area of the cartilage defect.
- [b] Average thickness of the reparative cartilage compared with that of the surrounding cartilage.